ACS APPLIED ENERGY MATERIALS

www.acsaem.org Article

Tuning Ternary Alloyed Nanoparticle Composition and Morphology by Exsolution in Double Perovskite Electrodes for CO_2 Electrolysis

Andrés López-García, Laura Almar, Sonia Escolástico, Ana B. Hungría, Alfonso J. Carrillo,* and Jose Manuel Serra*

Cite This: *ACS Appl. Energy Mater.* 2022, 5, 13269−13283 Read Online

ACCESS | Metrics & More | Article Recommendations | Supporting Information

ABSTRACT: The intermittent nature of renewable energy resources makes imperative the development of efficient energy storage technologies. Solid oxide electrolysis cells (SOECs) are a promising alternative to energy conversion devices. SOECs can play an important role in the control of greenhouse gases by improving processes such as CO_2 electrolysis. In order to enhance SOEC performance, exsolution of metal nanoparticles is emerging for the catalytic surface functionalization of electrodes, preventing sintering issues related to classical impregnation methods and enabling tailoring specific catalytic functions. In this work, a medium-entropy, double perovskite system $Sr_xFeCo_{0.2}Ni_{0.2}Mn_{0.1}Mo_{0.5}O_{6-\delta}$ (x = 2.0, 1.9, and 1.8) was studied. We provide evidence of Fe−Co−Ni ternary alloyed exsolved nanoparticles, revealing that the alloy composition can be tuned by adjusting the reducing conditions. Exsolution temperature is critical for Fe content in nanoparticles, increasing as temperature increases, but Ni and Co are not significantly affected. Temperature adjustments allowed control over nanoparticle size and population, shrinking and growing, respectively, as temperature decreases. In contrast to what is usually described, A-site deficiency resulted in a decrease in nanoparticle exsolution because of NiO phase formation in x = 1.9 and 1.8, so that the x = 2.0 compound outperformed both non-stoichiometric materials, showing significantly larger populations. The three compounds exhibit important conductivity under both oxidizing and reducing atmospheres, which makes them promising electrodes. The $Sr_2FeCo_{0.2}Ni_{0.2}Mn_{0.1}Mo_{0.5}O_{6-\delta}$ material was integrated as a cathode in an asymmetrical electrolyte-supported cell, and its electrochemical performance under CO_2 electrolysis conditions was studied. Our results showed a boost in electrocatalytic activity upon exsolution at 600 °C when compared to the fuel electrode without exsolved nanoparticles or exsolved at 800 °C, where the appearance of the secondary Ruddlesden-Popper phase was observed. Overall, here, we proved the possibility of obtaining ternary alloy exsolved nanoparticles and tuning their composition to enhance the performance of SOEC devices, paving the path for optimized metal-alloyed exsolved nanoparticle design, which might extend its applicability to other electrocatalytic processes in energy conversion and storage.

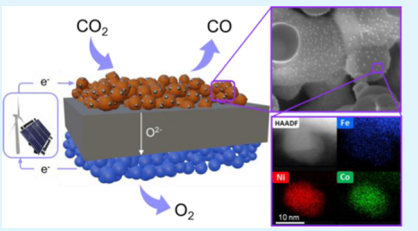

KEYWORDS: *exsolution, ternary alloys, CO_2 electrolysis, medium-entropy perovskites, metallic nanoparticles, SOEC*

INTRODUCTION

Renewable sources are at the core of the energy transition toward a more sustainable and decarbonized system. However, efficient energy storage systems are required to boost the implementation of renewable energy technologies and alleviate the inherent intermittence of wind and solar resources. In that sense, electrolysis emerges as a promising technology to convert the surplus renewable electricity into chemical energy.[1] Among the different electrolysis technologies, solid oxide electrolysis cells (SOECs) offer high efficiency and flexibility.[2,3] In SOECs, the CO_2 and/or H_2O reduction occurs at the triple-phase boundaries of the cathode or fuel electrode. The state-of-the-art fuel electrode is the cermet Ni-YSZ. However, Ni particles suffer from coking and tend to agglomerate in long-term operation, which eventually lowers their catalytic activity.[4]

Based on its enhanced sintering resistance, the exsolution method has gained great attention in the last years. Nanoparticles obtained through this synthetic route exhibit high stability over prolonged operation,[5−7] compared to other conventional methods such as impregnation, also enabling the tailoring of the catalytic function by controlling nanoparticles' composition, morphology, and interaction with the support. The fact that exsolved nanoparticles remain anchored into the backbone prevents nanoparticle sintering and coking formation,[8] guaranteeing stable catalytic activity. The mechanism of nanoparticle exsolution relies on the diffusion of metal cations contained in the oxide crystal lattice that, under reductive conditions, migrate to the surface nucleating as nanoparticles. Therefore, this implies that, by a proper material design, one can choose the composition of the exsolved nanoparticles, given that thermodynamics allows the nucleation of the metal cation into a

Received: June 11, 2022
Accepted: October 20, 2022
Published: November 8, 2022

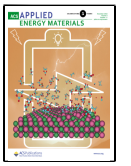

metal particle. Exsolution has been mainly explored using perovskite oxides as the host, which are a class of materials that have also been widely explored as ceramic electrode for SOECs.[5−7] Nevertheless, recently, metallic nanoparticle exsolution has been shown in other oxides such as ceria or Ce-based pyrochlores,[9−11] MgO,[12] or YSZ.[12] In addition, the versatility offered by the exsolution method expanded its use in other fields, such as catalysts for methane reforming[10,13−16] and CO_2 hydrogenation,[17−20] sensors,[21,22] or even resistive switching devices.[23]

Regarding SOEC applications, double perovskite oxides of the $Sr_2Fe_{1.5}Mo_{0.5}O_{6-\delta}$ formula have been widely explored as cathodes, in which B-site substitution has been commonly employed to tune their physicochemical properties. For instance, Jiang et al. fabricated the $Sr_2Fe_{1.4}Mn_{0.1}Mo_{0.5}O_{6-\delta}$ perovskite,[24] revealing that Mn incorporation enhanced the CO_2 reduction kinetics, increasing the oxygen transport and reducing the polarization resistance compared to $Sr_2Fe_{1.5}Mo_{0.5}O_{6-\delta}$. Moreover, B-site substitution has been employed to drive the exsolution of alloyed nanoparticles. For instance, Ni incorporation has led to the exsolution of $FeNi_3$ alloys in several studies.[25−28] Likewise, partial substitution of Fe by Co led to the exsolution of CoFe alloys,[29] which boosted the CO_2 electrolysis performance when compared to the parent perovskite. On the other hand, few studies have reported metallic Fe exsolution from $Sr_2Fe_{1.5}Mo_{0.5}O_{6-\delta}$ perovskites, due to a lower thermodynamic driving force of Fe to segregate to the surface as metal when compared to Co or Ni.[29] Only Chen et al. obtained exsolved nanoparticles by increasing the Fe content in the $Sr_2Fe_{1.5+x}Mo_{0.5}O_{6-\delta}$ formula.[30] Based on these reports, the $Sr_2Fe_{1.5}Mo_{0.5}O_{6-\delta}$ double perovskite class presents the required properties to study the tunability of the exsolved alloy compositions based on the ease to allocate several cations on the B-site. In this regard, the concept of high-entropy oxides has emerged,[31] which if applied to perovskites defines chemical compositions in which numerous cations are incorporated into the B-site position. For instance, Gazda et al. applied this concept to fabricate single-phase proton conducting perovskites.[32] Although system entropy (S_{conf}) increases with the addition of different elements to the same position (B-site, in this case), the maximum value is reached with equimolar fractions of these elements.[33] Then, a doped system based on $Sr_2Fe_{1.5}Mo_{0.5}O_{6-\delta}$ can predictably achieve a medium-entropy configuration, also with increased stability, and prevent instability issues, such as Sr segregation.[34] Here, we combine the concept of entropy-stabilized oxides to obtain double perovskite compositions that allow for the exsolution of multicomponent alloy nanoparticles. Besides Fe−Ni and Co−Fe alloys, few studies have reported ternary alloy exsolutions. Probably, the first report of a ternary alloy was by Zubenko et al. who exsolved Re−Ni−Fe alloys that showed enhanced catalytic activity for dry reforming of methane if compared to Re−Fe or Ni−Fe binary alloys.[15] More recently, and for the same application, Joo et al. reported Co−Fe−Ni exsolved nanoparticles.[35] However, in this case, the ternary alloy was obtained via topotactic exsolution, that is, Co and Ni were introduced in the B-site of the perovskite ($Pr_{0.5}Ba_{0.5}Mn_{0.85}Co_{0.05}Ni_{0.1}O_{3-\delta}$), while the Fe precursor was deposited on the surface of the oxide perovskite. Anyhow, their results indicated an enhanced catalytic activity of the ternary alloy with respect to the binary alloys and single exsolved metallic nanoparticles, illustrating the benefits of multicomponent alloy nanoparticles. In this regard and to the best of our knowledge, the only report of direct Co−Ni−Fe exsolution is the work of Mogni and co-authors[36] using $Sr_{0.93}(Ti_{0.3}Fe_{0.56}Ni_{0.07}Co_{0.07})O_{3-\delta}$ as a parent perovskite. However, despite the promise, there is still little understanding about the range of compositional variability of the ternary alloys and how, by adjusting the exsolution conditions, it might change.

In this work, the exsolution of Fe−Ni−Co alloys from $Sr_2FeCo_{0.2}Ni_{0.2}Mn_{0.1}Mo_{0.5}O_{6-\delta}$ (successively named Sr2) and its end use as an electrocatalyst in SOEC fuel electrodes is explored. Proof of direct ternary alloy exsolution from the $Sr_2Fe_{1.5}Mo_{0.5}O_{6-\delta}$ perovskite class for the first time is provided, identifying the adjustable parameters (A-site deficiency, time, and temperature) that allow tuning the composition of the exsolved alloyed nanoparticles, which have implications on the electrocatalytic activity for the CO_2 electrolysis.

EXPERIMENTAL METHODS

Material Synthesis. Powders of $Sr_xFeCo_{0.2}Ni_{0.2}Mn_{0.1}Mo_{0.5}O_{6-\delta}$ (x = 2.0, 1.9, and 1.8) were synthesized by a modified Pechini method. Metal precursors, $Sr(NO_3)_2$ (99%, Aldrich), $Fe(NO_3)_2{\cdot}9H_2O$ (98%, Aldrich), $Co(NO_3)_2{\cdot}6H_2O$ (99%, Aldrich), $Ni(NO_3)_2{\cdot}6H_2O$ (98.5%, Aldrich), $Mn(NO_3)_2{\cdot}4H_2O$ (98%, Aldrich), and $H_{24}Mo_7O_{24}N_6{\cdot}4H_2O$ (99%, Aldrich), in an appropriate molar ratio, were dissolved in distilled water. This dissolution was made together with citric acid (CA, 99%, Alfa Aesar) using a molar ratio of metal precursor:CA of 1:1.5, under constant stirring at 60 °C. Once dissolution was completed, ethylene glycol (EG, 99%, Aldrich-Merck) was added as a complexing agent (CA/EG ratio of 2/3 wt. %) and temperature was increased to 80 °C for faster water elimination, for 2 h. After most of the water was evaporated, the solution was transferred to a drying oven and heated to 220 °C overnight to cause gelification and further calcination of the formed gel. The solid obtained was grounded in an agate mortar to fine powder and then sintered at 1100 °C for 12 h. Exsolution treatments (2, 4, and 6 h) were carried out in a horizontal tubular furnace at different temperatures (800, 700, and 600 °C) under 5% H_2/Ar flow.

Physicochemical Characterization. To check the purity of obtained phases, X-ray diffractometry (XRD) was carried out with a PANalytical CubiX fast diffractometer using Cu $K_{\alpha1,2}$ radiation and a X'Celerator detector in Bragg−Brentano geometry. XRD patterns were recorded in a 2θ range of 20−80°, analyzed, and Rietveld-refined with X'Pert Highscore Plus software (version 3.0.0). Raman spectroscopy was performed with a Renishaw Raman spectrometer (New Mills, UK). Analyses were conducted at room temperature with a 514 nm laser equipped with an Olympus microscope and a CCD detector.

To study the morphology of the perovskites synthesized, before and after the exsolution process, scanning electron microscopy (SEM) characterization was carried out with a GeminiSEM 500 from Zeiss. Size and distribution of nanoparticles exsolved were obtained using ImageJ software (Version 1.52a).[37] Histograms of every sample were obtained in order to study the size and distribution of exsolved nanoparticles (Figure S4 in the Supporting Information). Depending on the exsolved material, between 200 and 900 nanoparticles were analyzed for each histogram.

Transmission electron microscopy (TEM) was also performed to study the composition of exsolved nanoparticles. The samples for these electron microscopy studies were carefully grinded in a mortar into a very fine powder and then deposited onto holey carbon-coated Cu grids. High-resolution scanning transmission electron microscopy analyses were performed at 200 kV on a double aberration-corrected FEI Titan^3 Themis 60-300 microscope. The instrument is equipped with a monochromatic, high-brightness XFEG source; a high-sensitivity Super-X-EDS system integrated by four window-less SDD detectors symmetrically arranged around the sample and the objective lens pole pieces. The acquisition of X-ray energy-dispersive spectroscopy (XEDS) maps was carried out using a beam current of 50 pA, convergence angle of 19 mrad, and 20 keV range. These analyses were performed for the $Sr_2FeCo_{0.2}Ni_{0.2}Mn_{0.1}Mo_{0.5}O_{6-\delta}$ (Sr2) samples after 4 h ex situ exsolution at 800 and 600 °C.

https://doi.org/10.1021/acsaem.2c01829
ACS Appl. Energy Mater. 2022, 5, 13269−13283

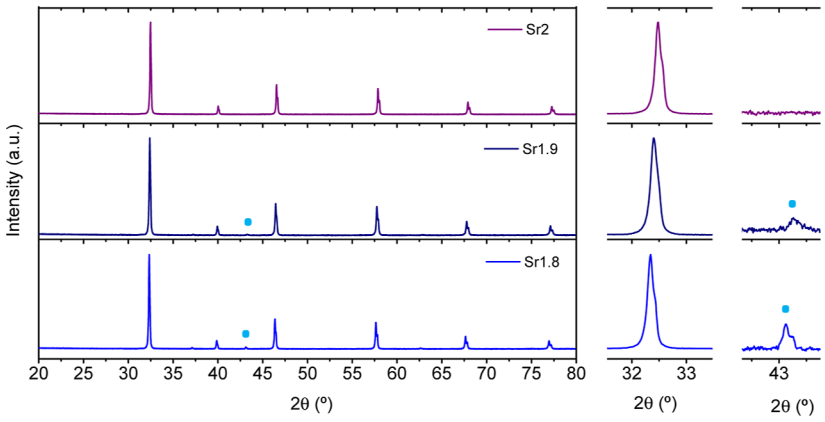

Figure 1. X-ray diffractograms of the as-synthesized $Sr_xFeCo_{0.2}Ni_{0.2}Mn_{0.1}Mo_{0.5}O_{6-\delta}$ (x = 2, 1.9, and 1.8) samples. Regions at 32 and 43° were zoomed out in order to depict in more detail the lattice expansion of the perovskite cubic phase and the appearance of NiO (light blue dots).

Temperature-programmed reduction (TPR) was examined from room temperature to 900 °C under 50 mL/min, 10% H_2/Ar flow in a 2910 Micrometrics system, measuring H_2 consumption with a thermal conductivity detector. X-ray photoelectron spectroscopy (XPS) analyses were carried out in a SPECS spectrometer with an MCD-9 detector, using a monochromatic Al Kα source, for materials as-synthesized and after exsolution processes. Exsolved samples were first in situ-treated with a 50 mL/min, 5% H_2/Ar flow at 400 °C for 2 h to eliminate possible passivation of nanoparticles. For spectral treatment, CasaXPS software was used. Thermogravimetric analyses (TG) were performed using NETSZCH STA 449 F3 equipment, measuring from room temperature to 1000 °C under synthetic air flow.

Electrochemical Measurements. Electrical conductivity was measured by a standard four-point DC technique, with silver wires and silver paste to improve contact between wires and samples. For this purpose, dense bars of each material were prepared. First, synthesized powders were mixed in an appropriate mass ratio with polyvinyl alcohol (99%, Merck) in distilled water. Then, rectangular bars were pressed under 30 kN for 3 min and sintered at 1450 °C for 10 h in air. Conductivity measurements were performed under synthetic air and 5% H_2/Ar flows from 800 °C to room temperature, with a cooling rate of 1 °C/min. A Keithley 2601 programmable current source and a multichannel Keithley 3706 multimeter were used.

For CO_2 electrolysis measurements, electrolyte-supported asymmetrical membranes with configuration Sr2 + CGO|CGO|ScSZ|CGO|LSCF were fabricated. The cells consisted of commercial $(ZrO_2)_{0.89}(Sc_2O_3)_{0.1}(CeO_2)_{0.01}$(ScSZ) electrolyte pellets of 150 μm thickness and 14 mm diameter (KERAFOL). To prevent interdiffusion of ionic species between electrodes and the electrolyte, thin buffer layers of $Ce_{0.8}Gd_{0.2}O_2$ (CGO) were used. These buffer layers were prepared via the sputtering method, using a Pfeiffer Classic 250 deposition system equipped with two RF (13.56 MHz) sources. Deposition conditions were 600 °C (sample temperature) and Ar/O_2 flow (5:1 ratio). CGO targets were sputtered onto ScSZ pellets (held by a rotational sample holder) from a 5 cm distance, with a 25 W RF power for 20 h. This procedure results in a dense barrier layer of about 400 nm thickness. For electrode preparation, $Sr_2FeCo_{0.2}Ni_{0.2}Mn_{0.1}Mo_{0.5}O_{6-\delta}$ powders were milled for 24 h in acetone, together with CGO (CerPoTech) (weight ratio of perovskite/CGO of 60:40). Then, the mixed powders were grounded in an agate mortar and sieved in a 200 μm sieve. These fine powders were used to obtain inks with a solution of 6% ethyl cellulose in terpineol. This terpineol-ethyl cellulose mixture was also employed to prepare $La_{0.6}Sr_{0.4}Co_{0.8}Fe_{0.2}O_{3-\delta}$ (LSCF) ink, previous 24 hour-milling in acetone and sieving. Sr2-CGO cathodes and LSCF anodes were screen-printed (two times each electrode, 9 mm of diameter) with intermediate drying in air at 80 °C. Then, 1050 °C calcination was performed for 5 h in air, resulting in 20 μm-thick electrodes. Finally, gold current collectors were painted on both electrode sides and sintered at 900 °C for 2 h in air.

Electrochemical measurements and CO_2 electrolysis experiments were performed in a double-chamber quartz-tube reactor placed inside a vertical furnace, supplying 15% CO_2/Ar flow (100 mL/min) to the cathode and air (60 mL/min) to the anode side at 800 °C. The temperature increase was carried out under Ar flow, and the cell was sealed to the reactor with an Ag-based alloy gasket. Cell tightness was ensured by continuously monitoring the nitrogen concentration in the cathode chamber, being 0.06% the maximum N_2 concentration detected. After ensuring gas tightness, the reduction treatment (with 5% H_2/Ar) in the cathode chamber was carried out for in situ exsolution for 4 h at 800 and 600 °C. Electrochemical impedance spectroscopy (EIS) spectra in a range of frequencies from 1 MHz to 0.03 Hz and an AC signal of 30 mV and $i-V$ curves were recorded using Solartron 1470E and 1455A FRA module equipment. To analyze impedance spectra, ZView fitting software was employed. The gas outlet during CO_2 electrolysis measurements was analyzed using a Micro-GC CP-4900 (Varian) gas chromatograph equipped with Molsieve5A and PoraPlot-Q glass capillary modules.

RESULTS

Evaluating Co–Fe–Ni Exsolution from $Sr_xFeCo_{0.2}Ni_{0.2}Mn_{0.1}Mo_{0.5}O_{6-\delta}$. Three samples with $Sr_xFeCo_{0.2}Ni_{0.2}Mn_{0.1}Mo_{0.5}O_{6-\delta}$ stoichiometry, in which x = 2, 1.9, and 1.8 (Sr2, Sr1.9, and Sr1.8, respectively), were synthesized through the Pechini method. Figure 1 shows the XRD data for the three materials as-synthesized (calcination at 1100 °C). The three samples exhibit a cubic double perovskite phase (space group $Fm\bar{3}m$) which is commonly obtained in similar compositions.[24] Importantly, even if five different cations occupied the B-site, a unique single phase is obtained for the stoichiometric compound. On the other hand, for the two other samples designed with A-site deficiency, NiO impurities were observed. These impurities were detected at the peaks located at ca. 43° (Figure 1). On the first basis, A-site deficiency was applied in order to study its effect on the nanoparticle exsolution, since it is commonly reported to increase the amount of exsolved nanoparticles from a perovskite backbone.[38] However, for the particular case of the double perovskite composition synthesized in this work, it has a detrimental effect as NiO segregation occurred in the as-synthesized samples. NiO segregation, which was previously observed in similar compositions,[39] was more accentuated with increasing A-site deficiency, with NiO concentrations of 1.3 and 3.5 % wt for Sr1.9 and Sr1.8, respectively. A-site deficiency also caused a lattice expansion, as denoted by the peak shift to lower 2θ values (Figure 1). The cell volume of the cubic phase was determined via Rietveld refinement (Figure S1). The cell volume values were

https://doi.org/10.1021/acsaem.2c01829
ACS Appl. Energy Mater. 2022, 5, 13269−13283

Table 1. Label, Composition, Crystal Phase, and Cell Volume of the As-synthesized $Sr_xFeCo_{0.2}Ni_{0.2}Mn_{0.1}Mo_{0.5}O_{6-\delta}$ Samples

label	formula	crystalline phase	cell volume (Å^3)	impurities (% wt)	Goldschmidt factor, t (−)
Sr2	$Sr_2FeCo_{0.2}Ni_{0.2}Mn_{0.1}Mo_{0.5}O_{6-\delta}$	cubic, $Fm\bar{3}m$	475.8		0.988
Sr1.9	$Sr_{1.9}FeCo_{0.2}Ni_{0.2}Mn_{0.1}Mo_{0.5}O_{6-\delta}$	cubic, $Fm\bar{3}m$	478.1	NiO (1.3)	0.963
Sr1.8	$Sr_{1.8}FeCo_{0.2}Ni_{0.2}Mn_{0.1}Mo_{0.5}O_{6-\delta}$	cubic, $Fm\bar{3}m$	480.4	NiO (3.5)	0.938

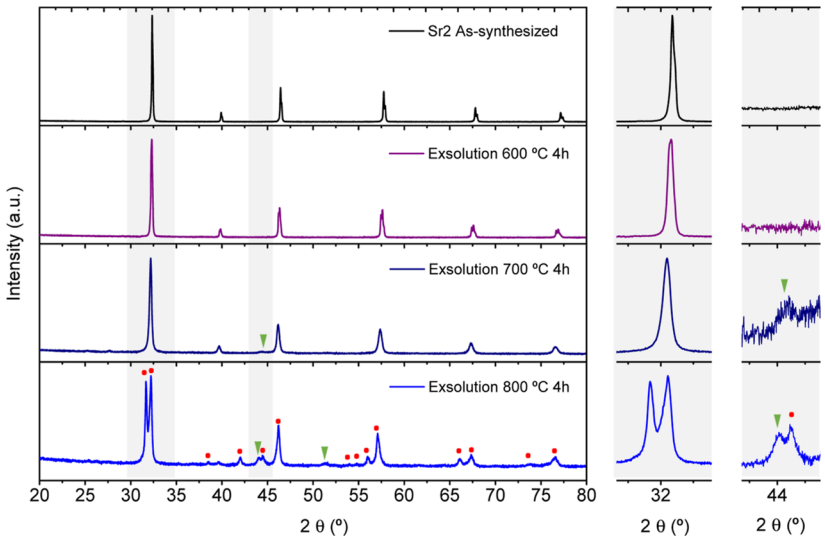

Figure 2. X-ray diffractograms of the $Sr_2FeCo_{0.2}Ni_{0.2}Mn_{0.1}Mo_{0.5}O_{6-\delta}$ sample before and after exsolution at 600, 700, and 800 °C. The regions at 32 and 44° were zoomed out in order to depict in more detail the appearance of the RP (red dots) and exsolved metallic phases (green triangle).

475.8, 478.1, and 480.4 Å^3 for Sr2, Sr1.9, and Sr1.8 samples, respectively. This lattice expansion is possibly ascribed to a change in oxidation states of transition metal cations present in the structure. A-site deficiency may be compensated, besides the increase in oxygen vacancies, with a reduction of these metallic atoms, thus increasing their ionic radii. This possibly explains the lattice expansion with A-site non-stoichiometry. These results agree with the work by Merkulov et al. They observed lattice expansion with A-site deficiency in $La_{0.5-x}Sr_{0.5}FeO_{3-\delta}$ and ascribed it to the generation of oxygen vacancies in order to compensate for A-site vacancies to fulfill the electroneutrality requirements.[40] In the literature, other studies have pointed out cation−oxygen bond rearrangement[41−43] upon creation of A-site vacancies, which can cause bond length enlargement, thus expanding the lattice. Thus, it seems that there is not a consensus on the mechanism that drives the lattice expansion upon the introduction of A-site vacancies. The previously described cubic phase can be foreseen through the Goldschmidt tolerance factor[44] (eq 1), which is useful to predict the stability of a perovskite

$$t = \frac{r_A + r_O}{\sqrt{2}(r_B + r_O)} \quad (1)$$

where r_A denotes the ionic radii of A-site cations; r_B denotes the proportional summation of ionic radii of B-site cations; and r_O denotes the ionic radius of oxygen. The Goldschmidt factor t for the three synthesized materials (Table 1) show values between 0.9 and 1.0, which means that the cubic phase is more likely to be stable,[45] in agreement with the former XRD results.

To check the high- or medium-entropy nature of synthesized perovskites, S_{conf} was calculated with the following equation[34] (eq 2)

$$S_{conf} = -R \sum_{i=1}^{n} X_i \cdot \ln X_i \quad (2)$$

where R is the ideal gas constant, n is the number of cations placed in the same position, and X_i is the molar fraction of these mentioned cations. If $1.0R \leq S_{conf} \leq 1.5R$, the system is considered as medium-entropy; in contrast, if $S_{conf} > 1.5R$, it is classified as high-entropy.[33,46] When this equation is applied to our materials, the result is $1.3R$, thus considered medium-entropy perovskites.

To analyze the resistance of these materials to carbonation, they were treated under a 15% CO_2 flow at 700 °C for 5 h. The XRD results after the CO_2 treatment are depicted in Figure S2, illustrating a high stability against carbonation under these specific conditions, since no additional peaks related to $SrCO_3$ (phase with the most intense peaks at 25−26°) were observed.

The next step is the analysis of the reduction treatment conditions and how they affect the nanoparticle exsolution. Special attention must be paid to the nanoparticle size and distribution, dispersion, and composition. First, the three synthesized samples were subjected to a reduction treatment under a 5% H_2/Ar atmosphere for 4 h at 800, 700, and 600 °C to study the temperature effect. Figure 2 shows the XRD for the Sr2 sample after reduction at 800−600 °C, benchmarked against the as-synthesized sample. As commented before, the Sr2 as-synthesized sample is a single-phase cubic double perovskite. This cubic phase is preserved after the reductive treatments at 600 and 700 °C. However, at 800 °C, there is a crystal phase transformation with the appearance of a major contribution of an A-site-rich Ruddlesden-Popper (RP) phase. The Sr_3FeMoO_7 RP-type phase is a tetragonal crystal structure, with the $I4/mmm$ space group. In addition to the RP phase, whose major peaks are at 31.6 and 32.2° (note that this last peak overlaps with the major peak of the double perovskite at 32.1°), and the main perovskite

https://doi.org/10.1021/acsaem.2c01829
ACS Appl. Energy Mater. 2022, 5, 13269−13283

Table 2. Crystal Phase Distribution and Cell Volume of the $Sr_xFeCo_{0.2}Ni_{0.2}Mn_{0.1}Mo_{0.5}O_{6-\delta}$ Samples, with x = 2, 1.9, and 1.8 Exsolved at 800 °C, 4 h in 5% H_2/Ar

sample	double perovskite, DP (%)	Ruddlesden-Popper, RP (%)	metallic alloy (%)	DP cell volume (Å^3)	RP cell volume (Å^3)
Sr2	39.5	56.4	4.1	491.7	314.7
Sr1.9	46.1	45.8	8.2	489.6	314.1
Sr1.8	65.6	25.5	8.9	488.8	314.3

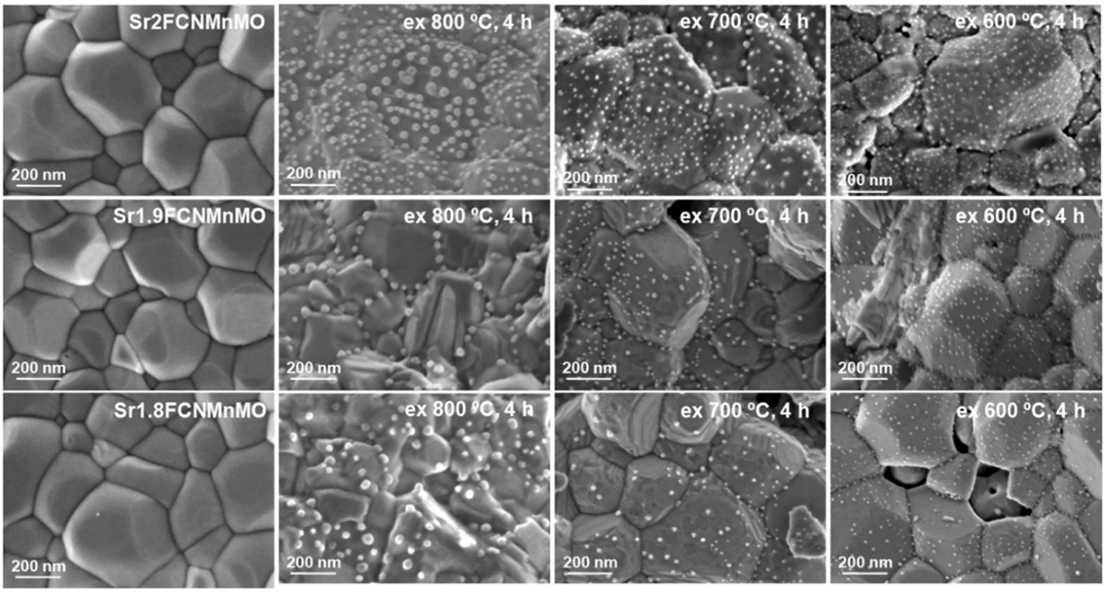

Figure 3. SEM micrographs of the $Sr_xFeCo_{0.2}Ni_{0.2}Mn_{0.1}Mo_{0.5}O_{6-\delta}$ samples with x = 2, 1.9, and 1.8 before (left panel) and after exsolution at 800, 700, and 600 °C for 4 h in a 5% H_2/Ar atmosphere.

phase, an additional phase was observed at 44.04°, which corresponds to the exsolved metallic phase. Quantification of the phases revealed the major presence of the RP phase, 56.4%, with 39.5% of the double perovskite and 4.1% of exsolved metallic nanoparticles. For the refinement of the exsolved metallic nanoparticles, a CoNi cubic alloy phase was used as a reference, since CoNiFe ternary alloys were not present in available crystallographic databases. In the following sections, more details will be provided about the exact composition of the exsolved alloy metallic nanoparticles. When lowering the exsolution treatment temperature down to 700 and 600 °C, the RP phase was not observed. Thus, the formation of the RP phase must occur in the 700−800 °C range. At 600 °C, the presence of the exsolved metallic phase was not inferred due to the detection limit; however, as it will be shown later, this does not exclude the presence of exsolved nanoparticles. However, at 700 °C, a minor peak at 44.3° is observed, ascribed to the exsolved metallic phase. This peak slightly shifted to higher 2θ values compared to the peak observed after exsolution at 800 °C, which might indicate that, depending on the treatment temperature, the composition of the exsolved nanoparticles might change.

Determination of the cubic double perovskite cell volume indicates a progressive lattice expansion with the increase in the reduction temperature. For instance, the cell volume for the Sr2 as-synthesized sample was 475.8 Å^3, and after the exsolution treatments, it was 484.9, 486.8, and 491.7 Å^3 for 600, 700, and 800 °C, respectively. The progressive lattice expansion with temperature correlates well with a higher reduction degree with increasing temperature, thus with the ionic radii enlargement of transition metallic cations due to their reduction. Sr1.9 and Sr1.8 were also treated under the same conditions, and the XRD data after the exsolution treatments are depicted in Figure S3 (Supporting Information). A similar trend is observed as for Sr2, the samples after exsolution at 600 and 700 °C maintain the double perovskite, and only after reduction at 800 °C, the RP phase appears. Interestingly, the peaks associated with the RP phase decreased in intensity with increasing A-site deficiency (Figure S3), indicating that by lowering the amount of Sr in the double perovskite, it is possible to delay the crystallographic transition. Table 2 shows the phase composition and cell volume values for Sr2, Sr1.9, and Sr1.8 samples after exsolution at 800 °C for 4 h, determined by Rietveld refinement. The amount of RP phase decreased from 56.4% for Sr2 to 45.8 and 25.5% for Sr1.9 and Sr1.8, respectively. Interestingly, the cell volume values for RP were similar for the three samples, around 314 Å^3, whereas the DP cell volume values decreased with increasing A-site deficiency (Table 2). It should be noted that the A-site-deficient as-synthesized samples were already expanded with respect to Sr2 (Table 1).

Regarding the region at which the metallic phase appears, some differences were observed with respect to the Sr2 sample. For instance, for Sr1.9 and Sr1.8, a peak at ca. 44.5° appeared after exsolution at 600 °C, which slightly shifted to 44.4° when the reductive treatment occurred at 700 °C. This peak is ascribed to metallic Ni.[47] However, it is important to note here that both Sr1.9 and Sr1.8 samples presented NiO impurities in the parent material. Thus, we ascribe the emergence of Ni in Sr1.9 and Sr1.8 after the treatment at 600 and 700 °C, respectively, to the reduction of the NiO phase, rather than to the exsolution of metallic Ni from the bulk, since at these temperatures, the exsolved nanoparticles would present low

https://doi.org/10.1021/acsaem.2c01829
ACS Appl. Energy Mater. 2022, 5, 13269−13283

particle size, hindering its detection by XRD in our equipment (as it is the case for Sr2). Interestingly, the amount of metallic phase increased for Sr1.9 (8.2%) and Sr1.8 (8.9%), with respect to Sr2 (4.1%) after exsolution at 800 °C (Table 2). However, this increase for both A-site-deficient materials might be triggered by the presence of metallic Ni obtained by the reduction of NiO present in the as-synthesized materials (Figure 1).

In order to study the morphology of the synthesized materials, SEM was performed for each sample: as-synthesized and after 4 h exsolution treatment at 800, 700, and 600 °C (Figure 3). The three as-synthesized materials present similar morphologies, with well-defined grain boundaries and particle sizes between about 50 and 350 nm. No remarkable secondary phases can be appreciated, despite the demonstrated presence of NiO in Sr1.9 and Sr1.8 samples, but in a very minor percentage. After the reductive treatment in a 5% H_2/Ar atmosphere, a morphological change occurs, caused by the exsolution of spherical nanoparticles. Focusing on the case of stoichiometric material, Sr2, in Figure 3, it can be appreciated that a remarkable amount of exsolved nanoparticles cover the surface of the perovskite oxide, regardless of the temperature treatment. After 800 °C exsolution, these nanoparticles exhibit a mean size of 21.3 nm and a population of 550 μm^{-2}. It is worth noting that after this 800 °C reducing treatment, due to the formation of the RP phase, some minor morphology changes can be appreciated, specifically affecting the grain boundaries. They appear less polygonal-shaped, especially observable for the stoichiometric Sr2 material. This fact is ascribed to the larger formation of the RP phase, compared to Sr1.9 and Sr1.8. As the exsolution temperature decreases, there is a significant reduction of the nanoparticles size (Figures 3 and 4a), reaching mean diameters of 11.6 nm at 700 °C and 8.9 nm at 600 °C. Decreasing exsolution temperature also has a clear effect on the nanoparticle population (Figure 4b), increasing to values of 1200 and 1800 μm^{-2} at 700 and 600 °C, respectively. This temperature-dependent behavior over size and population has been already observed in previous studies,[47,48] depending on the exsolved material. On the other hand, non-stoichiometric compounds exhibited counterintuitive results regarding population. As mentioned in previous sections, a growth in the amount of exsolved nanoparticles is usually expected by introducing A-site deficiency. Nevertheless, an evident drop in the amount of exsolved nanoparticles is observed in both non-stoichiometric materials (Figure 4b), especially when compared to Sr2. These results can be explained by the previously mentioned NiO phase segregation, which acts detrimentally to the exsolution process in this case, causing a descending trend in nanoparticle population as A-site deficiency increases. In fact, the remarkable difference between Sr2 and non-stoichiometric compound (Sr1.9 and Sr1.8) nanoparticle dispersion after exsolution at 800 °C can be seen at a glance in Figure 3. NiO segregation also changes the relation (Sr/B-site cations), thus affecting the real A-site deficiency. This results in (1.9/1.93) relation for Sr1.9 and (1.8/1.812) for Sr1.8, which means lower non-stoichiometry degree. Consequently, it has been proved that the presence of NiO plays a critical role in the exsolution of these materials. It is worth mentioning the formation of cavities, as seen in the 600 °C exsolution of the Sr1.8 material, due to the reduction of NiO to metallic Ni. Later sections will show that Ni is the main component forming these metal nanoparticles, which explains the great impact the lack of Ni to exsolve can have. Ni is playing, in fact, a relevant role in exsolving other metallic atoms, especially those with low segregation energy, in this case, Fe. It is seen that co-exsolution of Fe in this family of double perovskites with other metallic atoms can enhance the exsolution process.[49] On the other hand, B-site Ni-doping in $Sr_2Fe_{1.5}Mo_{0.5}O_{6-\delta}$ proved to have a direct impact on the reducibility of B-site cations, promoting it, which lastly would maximize exsolution of metallic NPs.[26] Interestingly, it can be seen for the Sr1.9 sample that the exsolved nanoparticles generated after the 800 °C treatment tend to grow and nucleate in the grain boundaries of the oxide particles.[6] Regarding nanoparticle size, there is an identical tendency in Sr1.9 and Sr1.8, compared to Sr2: nanoparticles becoming smaller as exsolution temperature decreases. Although mean sizes are similar for all three materials with 600 °C exsolution, a soft growing trend with A-site deficiency can be observed at 700 and 800 °C exsolution (Figure 4a). A larger amount of exsolved nanoparticles suggests a favored nucleation process. Consequently, as population decreases, with equal exsolution time (4 h), it is predictable certain, proportional growing of formed nanoparticles when there is no more nucleation. This might be the reason of larger nanoparticles when increasing A-site deficiency, with identical exsolution time and temperature. In summary, the Sr2 material outperformed Sr1.9 and Sr1.8 in terms of higher exsolved nanoparticle population, at any of the temperatures tested and lower nanoparticle sizes.

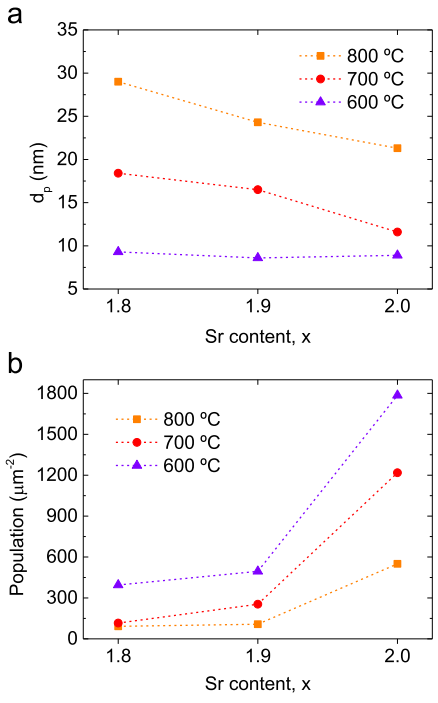

Figure 4. Influence of the A-site deficiency, x in $Sr_xFeCo_{0.2}Ni_{0.2}Mn_{0.1}Mo_{0.5}O_{6-\delta}$ in the (a) particle size (d_p) and (b) population of the exsolved nanoparticles after exsolution treatments at 800, 700, and 600 °C.

Next, the effect of the exposure time on the nanoparticle exsolution was assessed for the Sr2 material. Figure S5 shows the SEM images of the Sr2 sample exsolved at 800 °C after 2, 4, and 6 h. The morphology of the three exsolved samples looks similar, with very minor differences in terms of particle size and dispersion (Table S1). For instance, the particle size slightly increases with exposure time from 20.4 to 21.3 and 24.3 nm for 2, 4, and 6 h, respectively, of hydrogen treatment at 800 °C.

https://doi.org/10.1021/acsaem.2c01829
ACS Appl. Energy Mater. 2022, 5, 13269−13283

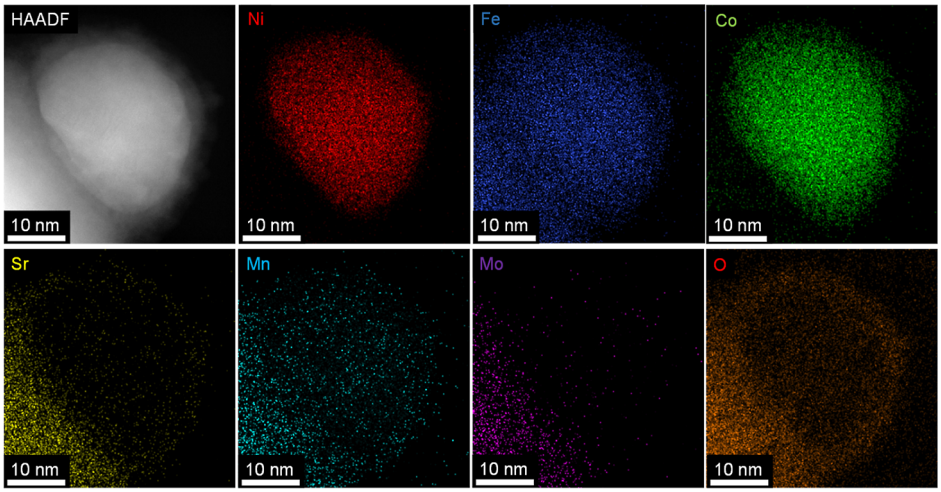

Figure 5. HAADF-STEM image and XEDS maps of a Fe−Co−Ni ternary alloy nanoparticle exsolved from $Sr_2FeCo_{0.2}Ni_{0.2}Mn_{0.1}Mo_{0.5}O_{6-\delta}$ at 800 °C, 4 h, and 5% H_2/Ar atmosphere.

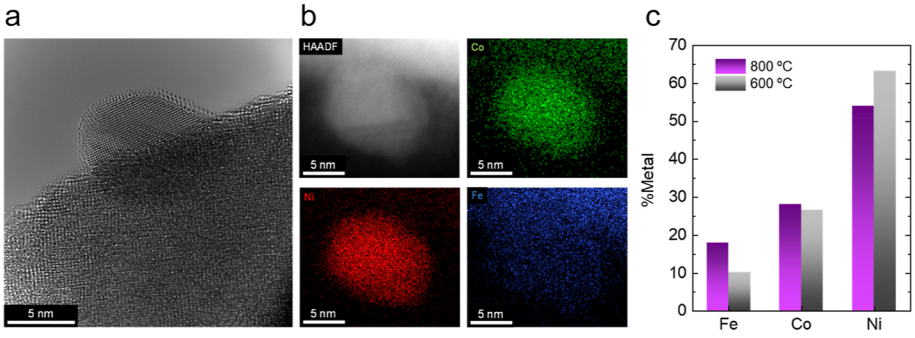

Figure 6. (a) HR TEM image and (b) HAADF-STEM and XEDS mapping images of an FeCoNi ternary alloy nanoparticle exsolved from $Sr_2FeCo_{0.2}Ni_{0.2}Mn_{0.1}Mo_{0.5}O_{6-\delta}$ at 600 °C, 4 h, and 5% H_2/Ar atmosphere. (c) Comparison of the composition of two ternary alloy nanoparticles exsolved at two different temperatures. (% metal = $(A_{Me}/A_{Ni} + A_{Fe} + A_{Co}) \times 100$; where A_{Me} is the atomic fraction measured by XEDS and Me = Ni, Fe, or Co).

Regarding the exsolved nanoparticle population, the maximum was obtained at 4 h (550 particles μm^{-2}), whereas after 2 and 6 h, it was 537 and 532 particles μm^{-2}, respectively. Based on these data, treatment after 4 h was chosen as it provided the optimum tradeoff between particle size and dispersion. Figure S6 shows a comparison of the XRD for these samples. All of them presented a mixture of double perovskite (DP) and Ruddlesden-Popper (RP) phases and the metallic alloy contribution. Table S1 shows a quantification of the amount of each phase, depicting the progressive decrease in the DP phase with increasing exsolution treatment time. The DP phase shows a progressive lattice expansion upon 4 h (491.7 $Å^3$); however, at 6 h, the cell volume slightly decreased to 491.2 $Å^3$, suggesting that a maximum cell expansion is reached at 4 h.

After identifying the effects that time and temperature have on the nanoparticle size and dispersion, we focused on understanding, with more detail, the nature of the exsolved nanoparticles. For this reason, a detailed high-resolution TEM analysis of the exsolved nanoparticles was performed to elucidate their composition and the possible effects that the temperature treatment has on it. From this point on, our analyses will be solely focused on the Sr2 material for two main reasons: its lack of NiO segregation in the parent material and the higher dispersion of exsolved nanoparticles if compared with Sr1.9 and Sr1.8.

Figure 5 depicts the HAADF-STEM image and the XEDS maps of a nanoparticle exsolved from the Sr2 sample at 800 °C (4 h, 5% H_2/Ar). First, in the HAADF image, the nanoparticle anchoring can be observed, typical of the exsolution method. This image illustrates that the particle is partially embedded on the oxide surface, which provides it with high resistance to agglomeration and sintering. The XEDS mapping indicates that the nanoparticle is formed by Ni, Fe, and Co. Thus, we have the first confirmation of ternary alloy exsolution from $Sr_2FeCo_{0.2}Ni_{0.2}Mn_{0.1}Mo_{0.5}O_{6-\delta}$, corroborating the XRD results of Figure 2. To obtain more information about the composition of the exsolved nanoparticle and the perovskite backbone after exsolution, an area scan comparing the inner region of the exsolved and the oxide in the proximity to the surface was performed (Figure S7 in the Supporting Information). The elemental analysis of the inner region shows that it is mainly composed of Ni (atomic fraction of 43.3%) followed by Co (22.5%) and Fe (14.4%). The rest is mainly oxygen, since there is a layer covering the nanoparticle that, according to the maps and the line scan (Figure S7), is formed by Co, Fe, and O. This corresponds to the passivation of the metallic nanoparticle, which was stored under ambient conditions, which seems to be covered by a thin layer (less than 5 nm) of a Co−Fe spinel oxide. Importantly, the XEDS maps and the line scan of Figure S7 illustrate the absence of Ni in the passivation layer, indicating a lower tendency to be oxidized than Fe or Co. On the other hand,

https://doi.org/10.1021/acsaem.2c01829
ACS Appl. Energy Mater. 2022, 5, 13269−13283

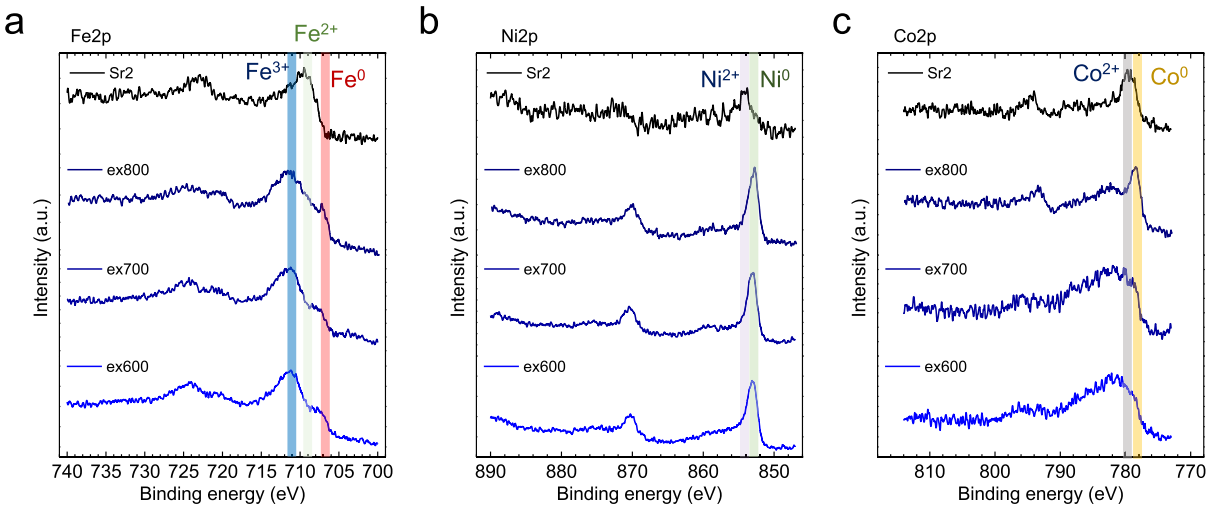

Figure 7. X-ray photoemission spectra of (a) Fe 2p, (b) Ni 2p, and (c) Co 2p core levels of $Sr_2FeCo_{0.2}Ni_{0.2}Mn_{0.1}Mo_{0.5}O_{6-\delta}$ before and after exsolution at 800, 700, and 600 °C for 4 h in a 5% H_2/Ar atmosphere.

Ni is the major component of the exsolved nanoparticle, doubling and tripling the atomic fraction of Co and Fe, respectively. When looking at the elemental composition of the oxide support surface at the proximity of the nanoparticle, it can be observed that the amount of Co and Ni is almost negligible. Thus, it seems that the exsolution process caused the depletion of both elements from the perovskite backbone, as the almost total amount of Ni and Co leave the perovskite backbone in the form of exsolved nanoparticles. It should be noted here that after exsolution at 800 °C, the oxide backbone is a mixture of the RP and DP phases; however, with the present data, we could not discern so far differences in the parent oxide and if it would have any effect on the exsolution.

In summary, the first proof of ternary metallic alloy nanoparticle exsolution from a Sr−Fe−Mo-based system is provided. We found that (1) Ni is the main component of the alloy followed by Co and Fe, (2) the passivation layer is formed by a Co−Fe oxide, and (3) there is depletion of Ni and Co from the parent oxide caused by the exsolution process.

To assess the effect of temperature on the elemental composition of the exsolved nanoparticles, an HRTEM analysis of the Sr2 sample exsolved at 600 °C (4 h, 5% H_2/Ar) was performed. Figure 6a depicts an HRTEM micrograph of such a sample, showing an exsolved nanoparticle embedded in the parent perovskite backbone. The nanoparticle, which is about 10 nm of diameter, shows in this case a much thinner layer of passivation. Figure 6b shows the HAADF-STEM and XEDS maps for a nanoparticle exsolved under the aforementioned conditions, illustrating that with exsolution at 600 °C, it is also possible to obtain a ternary metallic alloy composed by Ni, Co, and Fe. However, when scrutinizing the atomic fraction of each element with XEDS area analyses (Figure S8 in the Supporting Information), we could identify compositional differences with the nanoparticles exsolved at 800 °C. This comparison is summarized in Figure 6c. Here, a remarkable increase in the relative composition of Ni with respect to Fe and Co at 600 °C can be observed. For instance, at such a temperature, the amount of Ni is 2.4 and 6 times higher than the amount of Co and Fe, respectively, whereas at 800 °C, the Ni is 1.8 and 3 times the values of Co and Fe, respectively. Thus, it seems that the decrease in the exsolution temperature hinder the exsolution of Co and, especially, Fe. These results correlate well with DFT analyses provided by Lv et al.,[50] which pointed to a lower thermodynamic favorability for the exsolution of Fe. Here, we add a new level of adjustment driven by the careful control of the exsolution temperature. In the previous section, Figures 4 and 5, we illustrate how, by controlling the exsolution temperature, the nanoparticle size and dispersion can be adjusted. In addition, by proper adjustment of the temperature, the exsolved alloy composition can be tuned in a very simple manner. These could find potential applications in several catalytic processes in which, by adjusting the metallic alloy composition, it would be possible to increase the reaction conversion or selectivity to desired compounds.

To corroborate the nature of the exsolved nanoparticles, the materials were analyzed, before and after exsolution, with XPS (Figure 7). Here, we focused on the qualitative analyses of the metallic species that were present in the perovskite surface and exsolved nanoparticles, with special attention to the exsolution temperature treatment. Figure 7 depicts the XPS data for Fe 2p (Figure 7a), Ni 2p (Figure 7b), and Co 2p (Figure 7c). In all three cases, notorious changes upon material exsolution can be observed. Before exsolution, the Fe 2p spectra in the Sr2 sample are mainly dominated by Fe^{2+} and Fe^{3+} components (with $2p_{3/2}$ bands at ca. 709 and 710.7 eV, respectively).[51] However, upon exsolution, even at 600 °C, a $2p_{3/2}$ band around 706.75 eV appears which corresponds to metallic Fe.[51] This peak ascribed to metallic Fe increased in intensity with increasing exsolution temperature, which matches well with the EDX mapping results reported in the previous section, indicating that, by increasing the exsolution temperature, a higher amount of metallic Fe was present in the ternary alloy exsolved nanoparticles. Regarding the Ni 2p (Figure 7b) component, before exsolution, a minor presence of Ni^{2+} ($2p_{3/2}$ ca. 852.5 eV) was observed. After exsolution, at any of the three temperatures assayed, a strong peak ($2p_{3/2}$) at 851 eV was detected, which is ascribed to Ni metal. Opposite to Fe exsolution, XPS data showed a high presence of metallic Ni regardless of the temperature used for the exsolution treatment, pointing to an easier migration of Ni cations under reductive atmospheres and a higher driving force for metallic Ni exsolution. Finally, Co2p data showed a similar behavior to Fe. Before exsolution, the main band was ascribed to Co^{2+} $2p_{3/2}$ at 780 eV.[51] However, upon exsolution, a small band ($2p_{3/2}$) around 779 eV emerges at 600 and 700 °C of exsolution

https://doi.org/10.1021/acsaem.2c01829
ACS Appl. Energy Mater. 2022, 5, 13269−13283

treatment, which is ascribed to metallic Co. The intensity of this band increased notably when the exsolution treatment was performed at 800 °C, as observed for Fe. In conclusion, XPS data corroborated the EDX-SRTEM observations, pointing out to a compositional variability of the exsolved nanoparticles depending on the temperature of choice used for the exsolution treatment, that is, higher temperatures (800 °C) favored the exsolution of Co, and especially, Fe, which are present in lower quantities at 600 and 700 °C. On the other hand, Ni exsolution was affected to a lesser extent (if any) by temperature, and metallic Ni was easily detected by XPS at the three temperatures assayed. These results agree with TPR analysis performed (Figure S9), which shows that the reduction of Ni^{2+} to metallic Ni occurs at low temperature (between 360 and 400 °C), whereas metallic Fe and Co occur at temperature above 800 °C as it was inferred from the TPR analysis.[52,53]

Electrochemical Performance and Potential Applications. To discern the potential applications for the developed materials, conductivity measurements were performed under oxidizing and reducing conditions. Figure 8a shows the conductivity as a function of temperature in synthetic air. Conductivity increases with temperature for the three compounds below 400−500 °C (depending on the material) that are attributed to the small polaron hopping conduction mechanism, p-type conductivity. Above 500 °C, material conductivity lowers as temperature increases. This behavior is attributed to the increase in oxygen vacancies due to the loss of structural oxygen above 400 °C as it is inferred from the weight loss observed in the TG measurements (Figure S10). The formation of oxygen vacancies (that consumes electron holes) together with the reduction of Fe^{3+} to Fe^{2+} or Mo^{6+} to Mo^{5+} at higher temperature induces a drop in the charge carrier concentration and, consequently, in the conductivity. This behavior has been observed in other studies with similar materials[54,55] and other Sr perovskites.[56,57] Sr2 conductivity in air outperforms Sr1.9 and Sr1.8, reaching a maximum of about 26 S cm^{-1} at 600 °C. Conductivity as a function of temperature in 5% H_2 balanced Ar is plotted in Figure 8b. Materials were kept at 800 °C for 6 h, until conductivity was stable, indicating the proper exsolution and stabilization of the materials. In Figure S11, conductivity measurements before stabilization in 5% H_2 balanced Ar can be appreciated. The Sr2 material presents the highest conductivity, reaching values of 16 S cm^{-1} at 800 °C, followed by Sr1.8.

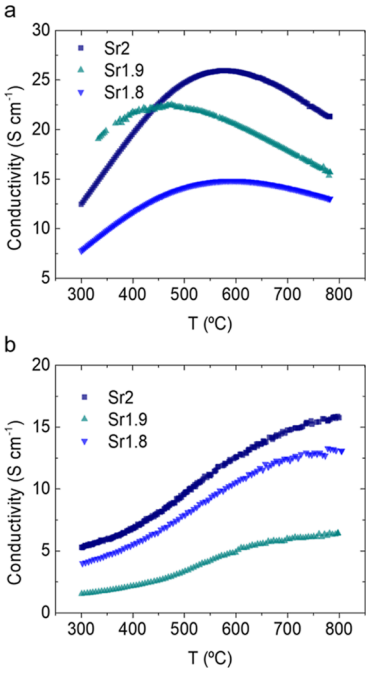

Figure 8. Conductivity measurements for the as-synthesized $Sr_xFeCo_{0.2}Ni_{0.2}Mn_{0.1}Mo_{0.5}O_{6-\delta}$ samples with x = 2, 1.9, and 1.8 in air (a) and 5% H_2/Ar (b) atmospheres.

Based on the physicochemical characterization results, the CO_2 electrolysis performance of the Sr2 material functionalized with in situ exsolved nanoparticles was analyzed, at both 800 and 600 °C (4 h treatment each), and its electrochemical activity against the oxide without exsolved nanoparticles, namely, without prior reduction treatment in H_2, was benchmarked. These electrolysis measurements were performed at 800 °C, in all cases. Given that exsolved nanoparticles can presumably grow at 800 °C after 600 °C exsolution, it is worth mentioning that the main idea of this reduction treatment temperature is to prevent the formation of the RP phase after exsolution, condition achieved after 600 °C exsolution, but not after 800 °C. Thus, the effect of this secondary phase can be evaluated, besides the differences between exsolution treatments. Figure 9 shows the cell architecture scheme and SEM micrographs of the different electrolyte-supported asymmetrical membranes with configuration Sr2 + CGO|CGO|ScSZ|CGO|LSCF, prepared to evaluate the Sr2 performance as the cathode for CO_2 electrolysis. Figure 9b depicts the cathode-electrolyte interface composed of the Sr2 + CGO porous composite electrode well connected to the CGO buffer layer of around 400 nm thickness. The fully assembled cell can be observed in Figure 9c, with a highly porous LSFC anode of about 20 μm thickness and the Sr2 + CGO cathode with 30 μm thickness, both showed proper attachment to the CGO buffer layers deposited by sputtering over the ScSZ electrolyte. In situ exsolution treatments were performed in the cathode chamber after sealing the cell to the reactor. Additionally, to evaluate the exsolution of the electrodes in cell configuration, reduction treatments were performed to half-cells and are shown in Figure 9d,e. These results demonstrate that the electrode showed nanoparticle exsolution when supported to the electrolyte, as can be seen in Figure 9d, for a cell exsolved at 800 °C, and in Figure 9e corresponding to a cell exsolved at 600 °C. For both treatments, nanoparticle sizes and populations are consistent with previous powder studies, showing similar d_p (around 22 and 10 nm after 800 and 600 °C exsolution, respectively) and nanoparticle distribution.

Figure S12 shows the current−voltage curves from the different SOECs fabricated and measured at the beginning of the experiment at 800 °C, with 15% CO_2 being supplied to the cathode chamber and air being supplied to the anode chamber. The $i-V$ curves exhibit non-linear behavior, commonly observed when perovskite oxides are used as electrodes for CO_2 electrolysis without premixing with CO.[24] For instance, we obtained a current density of about 400 mA cm^{-2} at an applied voltage of 1.5 V for non-exsolved and 600 °C exsolution membranes, although the 600 °C exsolved cell shows a slightly better performance at higher conversion rates (higher i). On the other hand, the exsolved cell at 800 °C showed the worst performance at higher current densities compared to both non-exsolved and 600 °C exsolved membranes. Such behaviors will be explained ahead, after EIS analyses and *post-mortem* characterization. Nevertheless, no large differences can be appreciated between the three samples; this is not surprising and

https://doi.org/10.1021/acsaem.2c01829
ACS Appl. Energy Mater. 2022, 5, 13269−13283

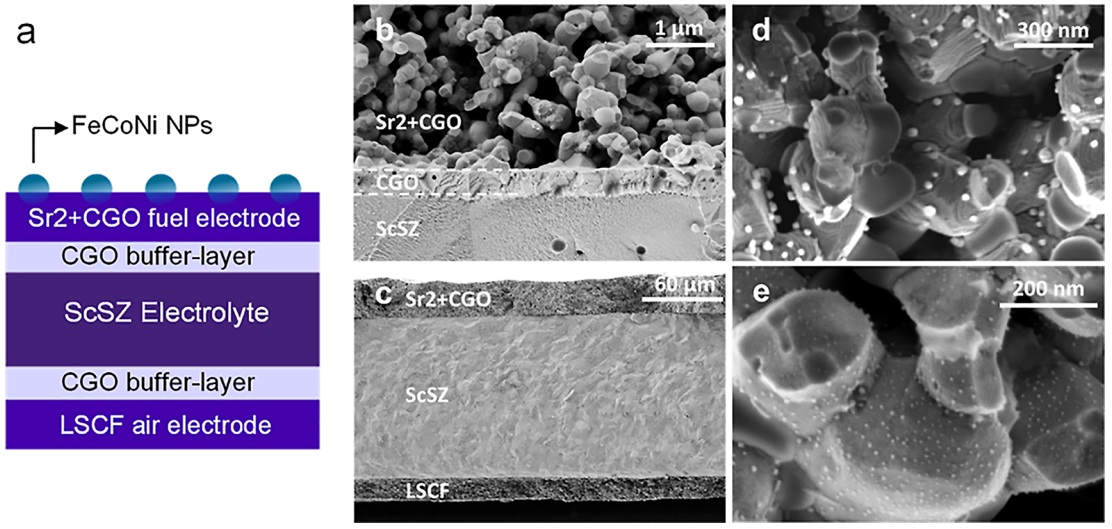

Figure 9. (a) Schematic of the fabricated SOEC with exsolved FeCoNi nanoparticles. SEM micrographs of the cross-section of Sr2-CGO|CGO|ScSZ|CGO|LSCF cells showing the (b) cathode-electrolyte interface and (c) whole cell, including the cathode, anode, and electrolyte. Sr2 + CGO cathode after exsolution treatment at (d) 800 and at (e) 600 °C.

can be explained by the large Ohmic resistance of the electrolyte-supported cells. Figure 10 plots the CO production and the

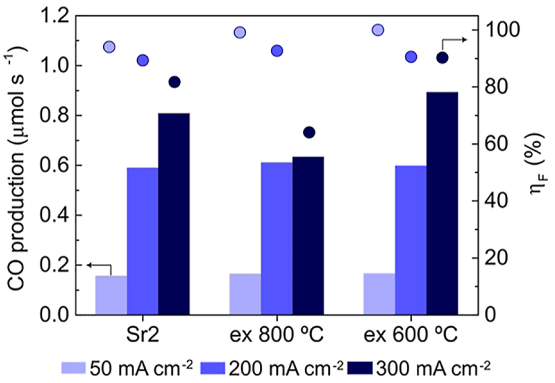

Figure 10. CO production rate and Faradaic efficiency for the different SOECs (Sr2 + CGO|CGO|ScSZ|CGO|LSCF), using 15% CO_2 flow in the cathode chamber and air in the anode chamber. All measures were performed at 800 °C.

corresponding Faradaic efficiency for the three samples by applying different current densities (50, 200, and 300 mA·cm^{-2}). CO production was very similar for the three samples at 50 and 200 mA·cm^{-2}, showing a slight improvement in exsolution-functionalized cells, compared to the non-exsolved one. At 300 mA·cm^{-2}, there is a remarkable change in the CO production trend. First, the 600 °C exsolved cell shows a larger and more evident improvement when compared to the non-exsolved and, especially, 800 °C exsolved membrane, which shows an important drop in its CO production. This drop can be subsequently seen in the Faradaic efficiency, arriving to its bottom (around 60%) at 300 mA·cm^{-2}, compared to 200 (90%) and 50 mA·cm^{-2} (almost 100%). This descending trend shows a deactivation of the 800 °C exsolved membrane that will be further explained with *post-mortem* characterization. Faradaic efficiency falls especially between 200 and 300 mA·cm^{-2}, which is consistent with the *i*−*V* curve for 800 °C exsolution (Figure S12). This drop in the Faradaic efficiency can be seen also in the non-exsolved membrane but strongly softer, reaching its lowest at 300 mA·cm^{-2} (80%) and remaining around 95 and 90% at 50 and 200 mA·cm^{-2}, respectively. This can be due to a deactivation process too, but clearly not as important as after 800 °C exsolution. The highest CO production and Faradaic efficiency were both obtained with the electrode functionalized with 600 °C exsolution treatment. After obtaining a 100% Faradaic efficiency at 50 mA·cm^{-2}, 90% is reached at both 200 and 300 mA·cm^{-2}, remaining stable in these *i* values.

To further study the drop in Faradaic efficiency affecting both exsolved electrodes and the remarkable decrease in the 800 °C exsolved cell, CO_2 electrolysis was performed for more than 80 h (Figure 11). These measurements were carried out at 1.2 V,

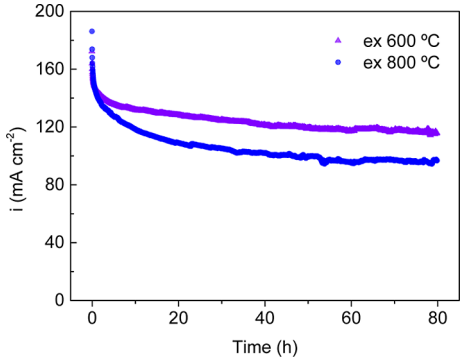

Figure 11. CO_2 electrolysis measurements at 800 °C for 80 h under constant voltage (1.2 V) for cells after in situ exsolution at 600 and 800 °C.

according to the *i*−*V* curves, remaining in the linear region for both cells. Over the first few hours of the experiment, in both cases, a clear drop in *i* can be seen. This decrease is larger for the 800 °C exsolved membrane, exhibiting lower *i* than the 600 °C exsolved cell after 80 h. After this initial fall, both cells show a slight loss of *i* with time. Between 30 and 80 h, an 8% *i* loss for both cells occur, which is far from the initial 20 h fall. *Post-mortem* SEM micrographs (Figure S13) demonstrate that the 800 °C exsolved membrane lost almost every nanoparticle on its surface after these experiments (CO_2 electrolysis and long-term analyses) and, the few remaining, exhibited great changes in

https://doi.org/10.1021/acsaem.2c01829
ACS Appl. Energy Mater. 2022, 5, 13269−13283

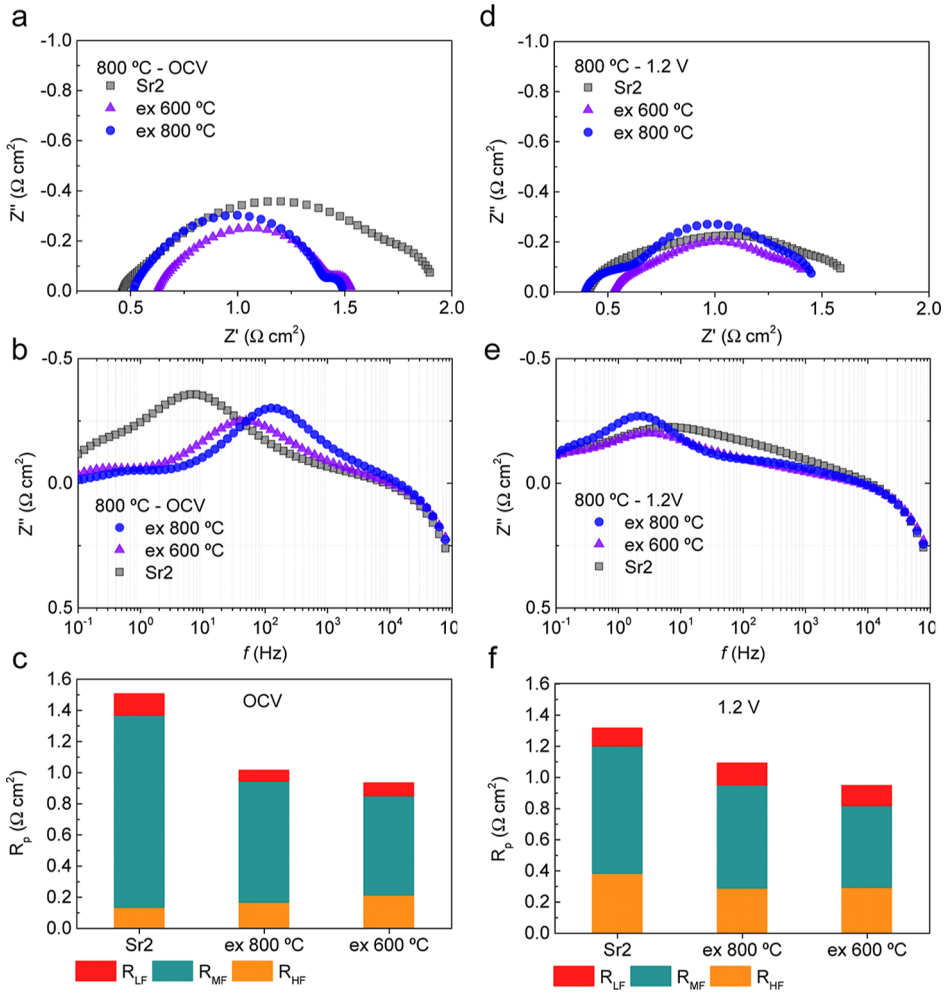

Figure 12. Nyquist and Bode plots from EIS measurements during CO_2 electrolysis experiments at 800 °C (a,b) at OCV and (d,e) at 1.2 V. Total R_p and its three contributions (R_{LF}, R_{MF}, and R_{HF}) at (c) OCV and (f) 1.2 V, for SOECs with the non-exsolved cathode, in situ exsolved cathode at 800 °C, and in situ exsolved cathode at 600 °C.

their morphology, not only size changes but shape variation too (Figure S13b,c). However, after measurements with the 600 °C cell, despite an important loss compared to the exsolution in powders (see Figure 3), a remarkably larger number of nanoparticles (Figure S13a) than in the 800 °C exsolved cell can be appreciated. Morphology changes are also observable, especially a growth of certain nanoparticles compared to the ones observed after 600 °C reduction treatment before electrolysis tests (from 10 to 30−35 nm growth). However, the spherical shape remains, unlike in the 800 °C exsolved cell. This growth of the NPs was predictable, according to the electrolysis temperature (800 °C). Morphology changes affecting Ni exsolved NPs have been observed by Kyriakou et al.,[58] after CO_2/H_2O co-electrolysis experiments without protection hydrogen flow. The injection of hydrogen is commonly used with Ni/YSZ electrodes to prevent Ni oxidation that may cause NP alterations. However, there is little information about *post-mortem* analyses in double perovskite oxides of the $Sr_2Fe_{1.5}Mo_{0.5}O_{6-\delta}$ family[50] after CO_2 electrolysis or other Ni exsolved perovskites[59] to carry out a proper comparison. Then, such differences in the stability of NPs between exsolved cells may be caused by certain instability of the cathode due to the phase change after 800 °C reduction, when the RP phase appears. In addition, *post-mortem* characterization revealed carbonate formation on the surface of the Sr2 + CGO cathode in situ exsolved at 800 °C, which can play a role in the degradation observed during cell testing (Figure S14). This $SrCO_3$ formation can be appreciated only after 800 °C exsolution, but not after the 600 °C reduction treatment. This fact suggests that the A-site rich RP phase can be susceptible to carbonation, seeing that the RP phase is no longer present in XRD diffractograms after CO_2 electrolysis and $SrCO_3$ peaks appear after 800 °C exsolution (Figure S14c). Thus, carbonation issues can be solved by lowering the exsolution temperature to prevent RP phase formation. In summary, the instability ascribed to the RP phase may explain the larger loss of NPs and consequently affect Faradaic efficiency, CO production, and *i*. All of them are remarkably decreased in the 800 °C exsolved membrane when compared to the 600 °C exsolved cell, which has no phase change due to the reduction treatment temperature. This larger loss of NPs, consequently, explains the bigger initial drop in the performance (Figure 11) of the 800 °C exsolved cell.

Electrochemical impedance spectroscopy (EIS) was performed to make a detailed analysis and comparison of the CO_2 electrolysis performance of the Sr2 + CGO different cathodes. Figure 12 shows the Nyquist (a) and Bode (b) plots of the different fabricated SOECs measured at 800 °C, open circuit voltage (OCV) at the beginning of the experiment. The impedance spectra were fitted by a complex non-linear least

https://doi.org/10.1021/acsaem.2c01829
ACS Appl. Energy Mater. 2022, 5, 13269−13283

square (CNLS) to the equivalent circuit $R_s(R_{LF}Q_{LF})(R_{MF}Q_{MF})$-$(R_{HF}Q_{HF})$ (LF, MF, and HF being low, medium, and high frequency, respectively) where R_s is the Ohmic resistance mostly attributed to the electrolyte, and the total polarization resistance of the cell can be calculated by the sum $R_p = R_{LF} + R_{MF} + R_{HF}$. This R_p and its three contributions can be observed in Figure 12c, for measurements at 800 °C and OCV. Noting that the characterized cells have an identical anode (LSCF) and electrolyte (CGO|ScSZ|CGO), R_p differences are attributed to the incorporated Sr2+CGO cathode. Lower R_p values of 1.02 and 0.93 Ω cm^2 are obtained for the cells in situ exsolved at 800 and at 600 °C at OCV, respectively, compared to the non-exsolved sample (1.51 Ω cm^2). The performance improvement can be ascribed to the presence of the exsolved alloyed nanoparticles, which emerged on the surface of the perovskites after the in situ exsolution treatment. This R_p reduction is clearly depicted in Figure 12c, which reveals that the in situ exsolved cell at 600 °C showed the lowest polarization resistance value. It also reveals an interesting trend related to medium frequency resistance contribution (R_{MF}), observable between 10^1 and 10^2 Hz in the Bode plot. This contribution clearly descends after exsolution, especially with 600 °C reduction treatment. This R_{MF} contribution, which corresponds to obtained capacitances between 10^{-2} and 10^{-1} F cm^{-2}, can be associated to the activation of the dissociative adsorption of CO_2 and to diffusion processes.[60,61] Figure 12d shows the Nyquist plot and Figure 12e shows the Bode plot of the SOECs measured when a voltage of 1.2 V was applied, same used for the 80 h CO_2 electrolysis measurements. The lowest R_p value (0.95 Ω cm^2) was, again, obtained for the in situ exsolved cell at 600 °C, followed by the 800 °C exsolved cell (1.09 Ω cm^2) and the non-exsolved cell (1.28 Ω cm^2), showing an R_p decrease with exsolution (Figure 12f), same trend as OCV impedances. In addition, the same decreasing trend with exsolution is observed in R_{MF}, which is consistent with OCV impedance measurements. Thus, these results reveal improved catalytic activity, especially after 600 °C exsolution, in line with the larger number of nanoparticles or reaction active sites and a more stable electrode when no RP phase is formed. Additional EIS studies were performed at 1.4 V (Figure S15). In all cases (Figure S14a,c,e), Nyquist plots were fitted to the equivalent circuit $R_s(R_{MF}Q_{MF})(R_{HF}Q_{HF})$. Apparently, R_{LF} descends drastically when increasing the applied voltage. On the other hand (Figure S14b,d,f), total R_p decreases for non-exsolved and 600 °C exsolved cells but not for the 800 °C exsolved cells. This fact is consistent with $i-V$ curves, that is, at 1.4 V, the 800 °C exsolved cell curve is no longer in the ohmic region, showing the worst performance at higher current densities, as explained previously. It is also worth noting that, for non-exsolved and 600 °C exsolved cells, R_{MF} decreases with increasing the applied voltage, which would be related to a better catalytic activity. Nevertheless, CO_2 electrolysis tests were performed at 1.2 V due to the degradation showed by the 800 °C exsolved cell at higher voltages.

As mentioned previously in this section, the three cells show large ohmic resistances (R_o) as electrolyte-supported cells. In fact, at 1.2 V, R_o represents 35, 26, and 22% of the total resistance for the exsolved cells at 600 and 800 °C and the non-exsolved one, respectively (0.51, 0.38 and 0.37 Ω cm^2). The variation in Ohmic resistance among cells can be ascribed to experimental differences related to sputtering buffer-layer deposition, that is, thickness, grain-morphology, and occluded porosity. From these results, it can be inferred that the use of a thinner electrolyte could improve the performance of these cells, especially in the 600 °C exsolved case. Changing the 150 μm-thick used electrolyte by a 10 μm-thick electrolyte instead would reduce 94% of the R_o contribution. This would directly affect the electrochemical performance of the cells by means of a potential growth in i: from 250 to 335 mA cm^{-2} at 1.2 V and from 400 to 535 mA cm^{-2} at 1.5 V for the 600 °C exsolved cell. This fact clearly exemplifies the need of further cell optimizations to improve the performance of these SOECs. Nevertheless, optimization of these cells relies not only on the used electrolyte but also on other parameters that need further optimization: changes in exsolved NPs and perovskite/CGO ratios of the fuel electrode composite or electrode thickness may have an important impact on the studied cells.

Finally, Figure S16 depicts the Raman spectra of the exsolved Sr2 + CGO cathodes (800 and 600 °C) after CO_2 electrolysis. The 600 °C exsolved cathode does not exhibit any carbon deposition feature, whereas a minor mode around 1560 cm^{-1} for the 800 °C exsolved cathode can be observed.

In summary, the exsolution route presented here shows a promising possibility to tune the composition and morphology of ternary alloyed nanoparticles to enhance the catalytic performance of SOEC devices. Further optimization of the cells and the reaction parameters is needed, in order to prevent NP loss during the measurements, accomplishing the full potential of the 600 °C exsolved Sr2 + CGO cathode. This surface-functionalized cathode showed the best electrochemical performance, especially due to the absence of RP phase formation, thus increasing its stability.

CONCLUSIONS

In this work, medium-entropy $Sr_xFeCo_{0.2}Ni_{0.2}Mn_{0.1}Mo_{0.5}O_{6-\delta}$ (x = 2, 1.9, and 1.8) electrodes were synthesized, and its surface functionalization via nanoparticle exsolution was evaluated. First, we observed that A-site deficiency was detrimental in terms of lower electric conductivity and exsolution extent, the latter caused by NiO phase segregation. The stoichiometric material (x = 2) showed remarkable exsolution with ca. 1800 particle μm^{-2} of 9 nm size when exsolution was performed at 600 °C for 4 h. When increasing the temperature, the population decreased and the nanoparticle size increased. In addition, exsolving at 800 °C led to the formation of a Ruddlesden-Popper (RP) secondary phase. Besides nanoparticle size and population, in this work, it is demonstrated that, by adjusting the exsolution conditions, namely, temperature, it is possible to tune the composition of the exsolved nanoparticles. Here, the medium-entropy double perovskite allows for the exsolution of ternary alloyed nanoparticles composed of Ni, Co, and Fe. STEM−EDX mapping revealed that the concentration of the elements in the exsolved nanoparticles follows the order Ni > Co > Fe. Importantly, by adjusting the temperature, the amount of Fe in the exsolved nanoparticle can be greatly increased, that is, a twofold increase in concentration was reached upon exsolution at 800 °C.

The implications of the exsolution temperature were also evaluated under CO_2 electrolysis conditions. Here, we found that the electrodes functionalized with exsolved nanoparticles created at 600 °C presented lower polarization resistance values with respect to the non-exsolved materials and after exsolution at 800 °C, which degraded after exposure to CO_2. This degradation is ascribed to the formation of $SrCO_3$, probably triggered by the presence of the secondary phase of RP. This phase also affects the stability of the cathode, leading to a greater performance loss

https://doi.org/10.1021/acsaem.2c01829
ACS Appl. Energy Mater. 2022, 5, 13269−13283

and morphology alteration of metallic NPs under electrolysis conditions, not observed for the electrode exsolved at 600 °C.

In summary, we proved ternary alloy nanoparticle exsolution from $Sr_2FeCo_{0.2}Ni_{0.2}Mn_{0.1}Mo_{0.5}O_{6-\delta}$ and the ability to easily tune its composition by adjusting the exsolution treatment conditions. This work could pave the way for the design of multicomponent nanoparticles *à la carte*, which might find potential applications in several energy storage and conversion technologies or thermocatalytic processes for fuel and chemical production.

■ ASSOCIATED CONTENT

Supporting Information

The Supporting Information is available free of charge at https://pubs.acs.org/doi/10.1021/acsaem.2c01829.

XRD patterns, nanoparticle size distribution histograms, SEM micrographs, STEM and XEDS elemental analyses, TPR curves, TGA curves, electrochemical performance comparisons, *post-mortem* SEM, XRD, and Raman analyses (PDF)

■ AUTHOR INFORMATION

Corresponding Authors

Alfonso J. Carrillo − *Instituto de Tecnología Química (Universitat Politècnica de València—Consejo Superior de Investigaciones Científicas), 46022 Valencia, Spain;* orcid.org/0000-0002-5576-9277; Email: alcardel@itq.upv.es

Jose Manuel Serra − *Instituto de Tecnología Química (Universitat Politècnica de València—Consejo Superior de Investigaciones Científicas), 46022 Valencia, Spain;* orcid.org/0000-0002-1515-1106; Email: jmserra@itq.upv.es

Authors

Andrés López-García − *Instituto de Tecnología Química (Universitat Politècnica de València—Consejo Superior de Investigaciones Científicas), 46022 Valencia, Spain;* orcid.org/0000-0001-9719-606X

Laura Almar − *Instituto de Tecnología Química (Universitat Politècnica de València—Consejo Superior de Investigaciones Científicas), 46022 Valencia, Spain*

Sonia Escolástico − *Instituto de Tecnología Química (Universitat Politècnica de València—Consejo Superior de Investigaciones Científicas), 46022 Valencia, Spain*

Ana B. Hungría − *Departamento de Ciencia de Materiales, Ingeniería Metalúrgica y Química Inorgánica, Universidad de Cádiz, 11510 Puerto Real, Spain;* orcid.org/0000-0002-4622-6967

Complete contact information is available at: https://pubs.acs.org/10.1021/acsaem.2c01829

Notes

The authors declare no competing financial interest.

■ ACKNOWLEDGMENTS

The project that gave rise to these results received the support of a fellowship from Spanish Government (RTI2018-102161 grant) and "la Caixa" Foundation (ID 100010434 and grant LCF/BQ/PI20/11760015). Authors acknowledge the use of instrumentation and the technical advice provided by the National Facility ELECMI ICTS, node "División de Microscopía Electrónica" at Universidad de Cádiz. We thank the support of the Electronic Microscopy Service of the Universitat Politècnica de València.

■ REFERENCES

(1) Lei, L.; Zhang, J.; Yuan, Z.; Liu, J.; Ni, M.; Chen, F. Progress Report on Proton Conducting Solid Oxide Electrolysis Cells. *Adv. Funct. Mater.* **2019**, *29*, 1903805.

(2) Zheng, Y.; Wang, J.; Yu, B.; Zhang, W.; Chen, J.; Qiao, J.; Zhang, J. A Review of High Temperature Co-Electrolysis of H_2O and CO_2 to Produce Sustainable Fuels Using Solid Oxide Electrolysis Cells (SOECs): Advanced Materials and Technology. *Chem. Soc. Rev.* **2017**, *46*, 1427−1463.

(3) Küngas, R. Review—Electrochemical CO_2 Reduction for CO Production: Comparison of Low- and High-Temperature Electrolysis Technologies. *J. Electrochem. Soc.* **2020**, *167*, 044508.

(4) Irvine, J. T. S.; Neagu, D.; Verbraeken, M. C.; Chatzichristodoulou, C.; Graves, C.; Mogensen, M. B. Evolution of the Electrochemical Interface in High-Temperature Fuel Cells and Electrolysers. *Nat. Energy* **2016**, *1*, 15014.

(5) Kim, J. H.; Kim, J. K.; Liu, J.; Curcio, A.; Jang, J.-S.; Kim, I.-D.; Ciucci, F.; Jung, W. Nanoparticle Ex-Solution for Supported Catalysts: Materials Design, Mechanism and Future Perspectives. *ACS Nano* **2021**, *15*, 81−110.

(6) Zhang, J.; Gao, M. M.-R.; Luo, J.-L. In Situ Exsolved Metal Nanoparticles: A Smart Approach for Optimization of Catalysts. *Chem. Mater.* **2020**, *32*, 5424−5441.

(7) Kousi, K.; Tang, C.; Metcalfe, I. S.; Neagu, D. Emergence and Future of Exsolved Materials. *Small* **2021**, *17*, 2006479.

(8) Neagu, D.; Oh, T.-S.; Miller, D. N.; Ménard, H.; Bukhari, S. M.; Gamble, S. R.; Gorte, R. J.; Vohs, J. M.; Irvine, J. T. S. Nano-Socketed Nickel Particles with Enhanced Coking Resistance Grown in Situ by Redox Exsolution. *Nat. Commun.* **2015**, *6*, 8120.

(9) Carrillo, A. J.; Navarrete, L.; Laqdiem, M.; Balaguer, M.; Serra, J. M. Boosting Methane Partial Oxidation on Ceria through Exsolution of Robust Ru Nanoparticles. *Mater. Adv.* **2021**, *2*, 2924−2934.

(10) Naeem, M. A.; Abdala, P. M.; Armutlulu, A.; Kim, S. M.; Fedorov, A.; Müller, C. R. Exsolution of Metallic Ru Nanoparticles from Defective, Fluorite-Type Solid Solutions $Sm_2Ru_xCe_{2-x}O_7$ To Impart Stability on Dry Reforming Catalysts. *ACS Catal.* **2020**, *10*, 1923−1937.

(11) Shen, X.; Chen, T.; Bishop, S. R.; Perry, N. H.; Tuller, H. L.; Sasaki, K. Redox Cycling Induced Ni Exsolution in $Gd_{0.1}Ce_{0.8}Ni_{0.1}O_2$ - $(Sr_{0.9}La_{0.1})_{0.9}Ti_{0.9}Ni_{0.1}O_3$ Composite Solid Oxide Fuel Cell Anodes. *J. Power Sources* **2017**, *370*, 122−130.

(12) Park, Y. S.; Kang, M.; Byeon, P.; Chung, S.-Y.; Nakayama, T.; Ko, T.; Hwang, H. Fabrication of a Regenerable Ni Supported NiO-MgO Catalyst for Methane Steam Reforming by Exsolution. *J. Power Sources* **2018**, *397*, 318−324.

(13) Carrillo, A. J.; Serra, J. M. Exploring the Stability of Fe−Ni Alloy Nanoparticles Exsolved from Double-Layered Perovskites for Dry Reforming of Methane. *Catalysts* **2021**, *11*, 741.

(14) Vecino-Mantilla, S.; Gauthier-Maradei, P.; Huvé, M.; Serra, J. M.; Roussel, P.; Gauthier, G. H. Nickel Exsolution-Driven Phase Transformation from an N=2 to an N=1 Ruddlesden-Popper Manganite for Methane Steam Reforming Reaction in SOFC Conditions. *ChemCatChem* **2019**, *11*, 4631−4641.

(15) Zubenko, D.; Singh, S.; Rosen, B. A. Exsolution of Re-Alloy Catalysts with Enhanced Stability for Methane Dry Reforming. *Appl. Catal., B* **2017**, *209*, 711−719.

(16) Carrillo, A. J.; Kim, K. J.; Hood, Z. D.; Bork, A. H.; Rupp, J. L. M. $La_{0.6}Sr_{0.4}Cr_{0.8}Co_{0.2}O_3$ Perovskite Decorated with Exsolved Co Nanoparticles for Stable CO_2 Splitting and Syngas Production. *ACS Appl. Energy Mater.* **2020**, *3*, 4569−4579.

(17) Steiger, P.; Kröcher, O.; Ferri, D. Increased Nickel Exsolution from $LaFe_{0.8}Ni_{0.2}O_3$ Perovskite-Derived CO_2 Methanation Catalysts through Strontium Doping. *Appl. Catal., A* **2020**, *590*, 117328.

(18) Burnat, D.; Kontic, R.; Holzer, L.; Steiger, P.; Ferri, D.; Heel, A. Smart Material Concept: Reversible Microstructural Self-Regeneration for Catalytic Applications. *J. Mater. Chem. A* **2016**, *4*, 11939−11948.
(19) Steiger, P.; Delmelle, R.; Foppiano, D.; Holzer, L.; Heel, A.; Nachtegaal, M.; Kröcher, O.; Ferri, D. Structural Reversibility and Nickel Particle Stability in Lanthanum Iron Nickel Perovskite-Type Catalysts. *ChemSusChem* **2017**, *10*, 2505−2517.
(20) Lim, H. S.; Kim, G.; Kim, Y.; Lee, M.; Kang, D.; Lee, H.; Lee, J. W. Ni-Exsolved La1-XCaxNiO3 Perovskites for Improving CO2 Methanation. *Chem. Eng. J.* **2021**, *412*, 127557.
(21) Li, X.; Dai, L.; He, Z.; Meng, W.; Li, Y.; Wang, L. Enhancing NH_3 Sensing Performance of Mixed Potential Type Sensors by Chemical Exsolution of Ag Nanoparticle on $AgNbO_3$ Sensing Electrode. *Sens. Actuators, B* **2019**, *298*, 126854.
(22) Li, X.; Dai, L.; He, Z.; Meng, W.; Li, Y.; Wang, L. In Situ Exsolution of PdO Nanoparticles from Non-Stoichiometric LaFeP-$d_{0.05}O_{3+\delta}$ Electrode for Impedancemetric NO_2 Sensor. *Sens. Actuators, B* **2019**, *298*, 126827.
(23) Spring, J.; Sediva, E.; Hood, Z. D.; Gonzalez-Rosillo, J. C.; O'Leary, W.; Kim, K. J.; Carrillo, A. J.; Rupp, J. L. M. Toward Controlling Filament Size and Location for Resistive Switches via Nanoparticle Exsolution at Oxide Interfaces. *Small* **2020**, *16*, 2003224.
(24) Jiang, Y.; Yang, Y.; Xia, C.; Bouwmeester, H. J. M. $Sr_2Fe_{1.4}Mn_{0.1}Mo_{0.5}O_{6-\delta}$ Perovskite Cathode for Highly Efficient CO_2 Electrolysis. *J. Mater. Chem. A* **2019**, *7*, 22939−22949.
(25) Du, Z.; Zhao, H.; Yi, S.; Xia, Q.; Gong, Y.; Zhang, Y.; Cheng, X.; Li, Y.; Gu, L.; Świerczek, K. High-Performance Anode Material $Sr_2FeMo_{0.65}Ni_{0.35}O_{6-\delta}$ with In Situ Exsolved Nanoparticle Catalyst. *ACS Nano* **2016**, *10*, 8660−8669.
(26) Wang, Y.; Liu, T.; Li, M.; Xia, C.; Zhou, B.; Chen, F. Exsolved Fe-Ni Nano-Particles from $Sr_2Fe_{1.3}Ni_{0.2}Mo_{0.5}O_6$ Perovskite Oxide as a Cathode for Solid Oxide Steam Electrolysis Cells. *J. Mater. Chem. A* **2016**, *4*, 14163−14169.
(27) Lv, H.; Lin, L.; Zhang, X.; Gao, D.; Song, Y.; Zhou, Y.; Liu, Q.; Wang, G.; Bao, X. In Situ Exsolved $FeNi_3$ Nanoparticles on Nickel Doped $Sr_2Fe_{1.5}Mo_{0.5}O_{6-\delta}$ Perovskite for Efficient Electrochemical CO_2 Reduction Reaction. *J. Mater. Chem. A* **2019**, *7*, 11967−11975.
(28) Meng, X.; Wang, Y.; Zhao, Y.; Zhang, T.; Yu, N.; Chen, X.; Miao, M.; Liu, T. In-Situ Exsolution of Nanoparticles from Ni Substituted $Sr_2Fe_{1.5}Mo_{0.5}O_6$ Perovskite Oxides with Different Ni Doping Contents. *Electrochim. Acta* **2020**, *348*, 136351.
(29) Lv, H.; Lin, L.; Zhang, X.; Song, Y.; Matsumoto, H.; Zeng, C.; Ta, N.; Liu, W.; Gao, D.; Wang, G.; Bao, X. In Situ Investigation of Reversible Exsolution/Dissolution of CoFe Alloy Nanoparticles in a Co-Doped $Sr_2Fe_{1.5}Mo_{0.5}O_{6-\delta}$ Cathode for CO_2 Electrolysis. *Adv. Mater.* **2020**, *32*, 1906193.
(30) Chen, L.; Xu, J.; Wang, X.; Xie, K. $Sr_2Fe_{1.5+x}Mo_{0.5}O_{6-\delta}$ Cathode with Exsolved Fe Nanoparticles for Enhanced CO_2 Electrolysis. *Int. J. Hydrogen Energy* **2020**, *45*, 11901−11907.
(31) Rost, C. M.; Sachet, E.; Borman, T.; Moballegh, A.; Dickey, E. C.; Hou, D.; Jones, J. L.; Curtarolo, S.; Maria, J.-P. Entropy-Stabilized Oxides. *Nat. Commun.* **2015**, *6*, 8485.
(32) Gazda, M.; Miruszewski, T.; Jaworski, D.; Mielewczyk-Gryń, A.; Skubida, W.; Wachowski, S.; Winiarz, P.; Dzierzgowski, K.; Łapiński, M.; Szpunar, I.; Dzik, E. Novel Class of Proton Conducting Materials—High Entropy Oxides. *ACS Mater. Lett.* **2020**, *2*, 1315−1321.
(33) Sarkar, A.; Wang, Q.; Schiele, A.; Chellali, M. R.; Bhattacharya, S. S.; Wang, D.; Brezesinski, T.; Hahn, H.; Velasco, L.; Breitung, B. High-Entropy Oxides: Fundamental Aspects and Electrochemical Properties. *Adv. Mater.* **2019**, *31*, 1806236.
(34) Shen, L.; Du, Z.; Zhang, Y.; Dong, X.; Zhao, H. Medium-Entropy Perovskites Sr(FeαTiβCoγMnζ)O3- as Promising Cathodes for Intermediate Temperature Solid Oxide Fuel Cell. *Appl. Catal., B* **2021**, *295*, 120264.
(35) Joo, S.; Kim, K.; Kwon, O.; Oh, J.; Kim, H. J.; Zhang, L.; Zhou, J.; Wang, J.; Jeong, H. Y.; Han, J. W.; Kim, G. Enhancing Thermocatalytic Activities by Upshifting the D-Band Center of Exsolved Co-Ni-Fe Ternary Alloy Nanoparticles for the Dry Reforming of Methane. *Angew. Chem., Int. Ed.* **2021**, *60*, 15912−15919.
(36) Santaya, M.; Troiani, H. E.; Caneiro, A.; Mogni, L. V. Ternary Ni−Co−Fe Exsolved Nanoparticles/Perovskite System for Energy Applications: Nanostructure Characterization and Electrochemical Activity. *ACS Appl. Energy Mater.* **2020**, *3*, 9528−9533.
(37) Schneider, C. A.; Rasband, W. S.; Eliceiri, K. W. NIH Image to ImageJ: 25 Years of Image Analysis. *Nat. Methods* **2012**, *9*, 671−675.
(38) Sun, X.; Chen, H.; Yin, Y.; Curnan, M. T.; Han, J. W.; Chen, Y.; Ma, Z. Progress of Exsolved Metal Nanoparticles on Oxides as High Performance (Electro)Catalysts for the Conversion of Small Molecules. *Small* **2021**, *17*, 2005383.
(39) Yu, N.; Jiang, G.; Liu, T.; Chen, X.; Miao, M.; Zhang, Y.; Wang, Y. Understanding the A-Site Non-Stoichiometry in Perovskites: Promotion of Exsolution of Metallic Nanoparticles and the Hydrogen Oxidation Reaction in Solid Oxide Fuel Cells. *Sustain. Energy Fuels* **2021**, *5*, 401−411.
(40) Merkulov, O. V.; Samigullin, R. R.; Markov, A. A.; Patrakeev, M. V. Impact of A-Site Cation Deficiency on Charge Transport in $La_{0.5-x}Sr_{0.5}FeO_{3-\delta}$. *Materials* **2021**, *14*, 5990.
(41) Qiu, Y.; Gao, R.; Yang, W.; Huang, L.; Mao, Q.; Yang, J.; Sun, L.; Hu, Z.; Liu, X. Understanding the Enhancement Mechanism of A-Site-Deficient La x NiO_3 as an Oxygen Redox Catalyst. *Chem. Mater.* **2020**, *32*, 1864−1875.
(42) Mineshige, A.; Izutsu, J.; Nakamura, M.; Nigaki, K.; Abe, J.; Kobune, M.; Fujii, S.; Yazawa, T. Introduction of A-Site Deficiency into $La_{0.6}Sr_{0.4}Co_{0.2}Fe_{0.8}O_{3-\delta}$ and Its Effect on Structure and Conductivity. *Solid State Ionics* **2005**, *176*, 1145−1149.
(43) Kharton, V.; Kovalevsky, A. V.; Tsipis, E. V.; Viskup, A. P.; Naumovich, E. N.; Jurado, J. R.; Frade, J. R. Mixed Conductivity and Stability of A-Site-Deficient Sr(Fe,Ti)O 3-δ Perovskites. *J. Solid State Electrochem.* **2002**, *7*, 30−36.
(44) Bartel, C. J.; Sutton, C.; Goldsmith, B. R.; Ouyang, R.; Musgrave, C. B.; Ghiringhelli, L. M.; Scheffler, M. New Tolerance Factor to Predict the Stability of Perovskite Oxides and Halides. *Sci. Adv.* **2019**, *5*, No. eaav0693.
(45) Jiang, S.; Hu, T.; Gild, J.; Zhou, N.; Nie, J.; Qin, M.; Harrington, T.; Vecchio, K.; Luo, J. A New Class of High-Entropy Perovskite Oxides. *Scr. Mater.* **2018**, *142*, 116−120.
(46) Sarkar, A.; Velasco, L.; Wang, D.; Wang, Q.; Talasila, G.; de Biasi, L.; Kübel, C.; Brezesinski, T.; Bhattacharya, S. S.; Hahn, H.; Breitung, B. High Entropy Oxides for Reversible Energy Storage. *Nat. Commun.* **2018**, *9*, 3400.
(47) Otto, S.-K.; Kousi, K.; Neagu, D.; Bekris, L.; Janek, J.; Metcalfe, I. S. Exsolved Nickel Nanoparticles Acting as Oxygen Storage Reservoirs and Active Sites for Redox CH_4 Conversion. *ACS Appl. Energy Mater.* **2019**, *2*, 7288−7298.
(48) Kyriakou, V.; Neagu, D.; Zafeiropoulos, G.; Sharma, R. K.; Tang, C.; Kousi, K.; Metcalfe, I. S.; van de Sanden, M. C. M.; Tsampas, M. N. Symmetrical Exsolution of Rh Nanoparticles in Solid Oxide Cells for Efficient Syngas Production from Greenhouse Gases. *ACS Catal.* **2020**, *10*, 1278−1288.
(49) Jo, S.; Han Kim, J.; Jeong, H.; Park, C.-h.; Won, B.-R.; Jeon, H.; Taek Lee, K.; Myung, J.-h. Exsolution of Phase-Separated Nanoparticles Via Trigger Effect Toward Reversible Solid Oxide Cell. *SSRN Electron. J.* **2022**, *323*, 119615.
(50) Lv, H.; Lin, L.; Zhang, X.; Song, Y.; Matsumoto, H.; Zeng, C.; Ta, N.; Liu, W.; Gao, D.; Wang, G.; Bao, X. In Situ Investigation of Reversible Exsolution/Dissolution of CoFe Alloy Nanoparticles in a Co-Doped $Sr_2Fe_{1.5}Mo_{0.5}O_{6-\delta}$ Cathode for CO_2 Electrolysis. *Adv. Mater.* **2020**, *32*, 1906193.
(51) Moulder, J.; Stickle, W.; Sobol, P.; Bomben, K. *Handbook of X-Ray Photoelectron Spectroscopy*; Physical Electronics Division, Perkin-Elmer Corporation, 1992.
(52) Feng, J.; Yang, G.; Dai, N.; Wang, Z.; Sun, W.; Rooney, D.; Qiao, J.; Sun, K. Investigation into the Effect of Fe-Site Substitution on the Performance of $Sr_2Fe_{1.5}Mo_{0.5}O_{6-\delta}$ Anodes for SOFCs. *J. Mater. Chem. A* **2014**, *2*, 17628−17634.
(53) Wang, H.; Dong, X.; Zhao, T.; Yu, H.; Li, M. Dry Reforming of Methane over Bimetallic Ni-Co Catalyst Prepared from La-

https://doi.org/10.1021/acsaem.2c01829
ACS Appl. Energy Mater. 2022, 5, 13269−13283

$(CoxNi_{1-x})_{0.5}Fe_{0.5}O_3$ Perovskite Precursor: Catalytic Activity and Coking Resistance. *Appl. Catal., B* **2019**, *245*, 302−313.
(54) Gou, M.; Ren, R.; Sun, W.; Xu, C.; Meng, X.; Wang, Z.; Qiao, J.; Sun, K. Nb-Doped $Sr_2Fe_{1.5}Mo_{0.5}O_{6-\delta}$ Electrode with Enhanced Stability and Electrochemical Performance for Symmetrical Solid Oxide Fuel Cells. *Ceram. Int.* **2019**, *45*, 15696−15704.
(55) Meng, J.; Liu, X.; Han, L.; Bai, Y.; Yao, C.; Deng, X.; Niu, X.; Wu, X.; Meng, J. Improved Electrochemical Performance by Doping Cathode Materials $Sr_2Fe_{1.5}Mo_{0.5-X}Ta_xO_{6-\delta}$ ($0.0 \leq x \leq 0.15$) for Solid State Fuel Cell. *J. Power Sources* **2014**, *247*, 845−851.
(56) Yáng, Z.; Harvey, A. S.; Infortuna, A.; Schoonman, J.; Gauckler, L. J. Electrical conductivity and defect chemistry of $Ba_xSr_{1-x}Co_yFe_{1-y}O_{3-\delta}$ perovskites. *J. Solid State Electrochem.* **2011**, *15*, 277−284.
(57) Wang, S. F.; Hsu, Y. F.; Huang, M. S.; Chang, C. W.; Cheng, S. Characteristics of Copper-Doped $SrFe_{0.75}Mo_{0.25}O_{3-\delta}$ Ceramic as a Cathode Material for Solid Oxide Fuel Cells. *Solid State Ionics* **2016**, *296*, 120−126.
(58) Kyriakou, V.; Neagu, D.; Papaioannou, E. I.; Metcalfe, I. S.; van de Sanden, M. C. M.; Tsampas, M. N. Co-Electrolysis of H_2O and CO_2 on Exsolved Ni Nanoparticles for Efficient Syngas Generation at Controllable H_2/CO Ratios. *Appl. Catal., B* **2019**, *258*, 117950.
(59) Kim, J.; Ferree, M.; Gunduz, S.; Millet, J.-M. M.; Aouine, M.; Co, A. C.; Ozkan, U. S. Exsolution of Nanoparticles on A-Site-Deficient Lanthanum Ferrite Perovskites: Its Effect on Co-Electrolysis of CO_2 and H_2O. *J. Mater. Chem. A* **2022**, *10*, 2483−2495.
(60) Almar, L.; Szász, J.; Weber, A.; Ivers-Tiffée, E. Oxygen Transport Kinetics of Mixed Ionic-Electronic Conductors by Coupling Focused Ion Beam Tomography and Electrochemical Impedance Spectroscopy. *J. Electrochem. Soc.* **2017**, *164*, F289−F297.
(61) Solís, C.; Navarrete, L.; Bozza, F.; Bonanos, N.; Serra, J. M. Catalytic Surface Promotion of Composite Cathodes in Protonic Ceramic Fuel Cells. *ChemElectroChem* **2015**, *2*, 1106−1110.

https://doi.org/10.1021/acsaem.2c01829
ACS Appl. Energy Mater. 2022, 5, 13269−13283